

# Journal of Geophysical Research: Solid Earth

## RESEARCH ARTICLE

10.1002/2017JB014423

**Key Points:**

- Mantle plume in West Antarctica compatible with presence of the ice sheet
- Presence of local plume impacts thermal conditions locally
- Additional observations necessary to refine basal conditions and structure of the plume

**Supporting Information:**

- Supporting Information S1

**Correspondence to:**

H. Seroussi,  
Helene.Seroussi@jpl.nasa.gov

**Citation:**

Seroussi, H., E. R. Ivins, D. A. Wiens, and J. Bondzio (2017), Influence of a West Antarctic mantle plume on ice sheet basal conditions, *J. Geophys. Res. Solid Earth*, 122, 7127–7155, doi:10.1002/2017JB014423.

Received 9 MAY 2017

Accepted 25 JUL 2017

Accepted article online 1 AUG 2017

Published online 4 SEP 2017

## Influence of a West Antarctic mantle plume on ice sheet basal conditions

**Helene Seroussi<sup>1</sup> , Erik R. Ivins<sup>1</sup> , Douglas A. Wiens<sup>2</sup> , and Johannes Bondzio<sup>3,4</sup> **

<sup>1</sup>Jet Propulsion Laboratory, California Institute of Technology, Pasadena, California, USA, <sup>2</sup>Department of Earth and Planetary Sciences, Washington University, Saint Louis, Missouri, USA, <sup>3</sup>Alfred Wegener Institute, Helmholtz Centre for Polar and Marine Research, Bremerhaven, Germany, <sup>4</sup>Department of Earth System Science, University of California, Irvine, California, USA

**Abstract** The possibility that a deep mantle plume manifests Pliocene and Quaternary volcanism and potential elevated heat flux in West Antarctica has been studied for more than 30 years. Recent seismic images support the plume hypothesis as the cause of Marie Byrd Land (MBL) volcanism and geophysical structure. Mantle plumes may more than double the geothermal heat flux above nominal continental values. A dearth of in situ ice sheet basal data exists that samples the heat flux. Consequently, we examine a realistic distribution of heat flux associated with a possible late Cenozoic mantle plume in West Antarctica and explore its impact on thermal and melt conditions at the ice sheet base. We use a simple analytical mantle plume parameterization to produce geothermal heat flux at the base of the ice sheet. The three-dimensional ice flow model includes an enthalpy framework and full-Stokes stress balance. As both the putative plume location and extent are uncertain, we perform broadly scoped experiments to characterize the impact of the plume on geothermal heat flux and ice sheet basal conditions. The experiments show that mantle plumes have an important local impact on the ice sheet, with basal melting rates reaching several centimeters per year directly above the hotspot. In order to be consistent with observations of basal hydrology in MBL, the upper bound on the plume-derived geothermal heat flux is 150 mW/m<sup>2</sup>. In contrast, the active lake system of the lower part of Whillans Ice Stream suggests a widespread anomalous mantle heat flux, linked to a rift source.

### 1. Introduction

Improved knowledge of the Antarctic basal geothermal heat flux,  $q_{\text{GHF}}$ , is important for sharpening our theoretical and numerical estimations of future ice sheet contribution to sea level rise. However, only a few direct in situ measurements have been conducted at the bottom of deep boreholes by Engelhardt [2004] and Fisher *et al.* [2015], due to the thick ice cover. Other inferences of geothermal heat flux come from tectonic correlation to surface wave maps [Shapiro and Ritzwoller, 2004], satellite magnetic data [Maule *et al.*, 2005], or interpretations of ice penetrating radar [Schroeder *et al.*, 2014]. While the important connection between heat and water has long been known to be critical to understanding processes beneath the Antarctic ice streams [e.g., Blankenship *et al.*, 1986], a growing interest in the basal hydrologic conditions beneath West Antarctic Ice Sheet (WAIS) has been motivated by both the discovery of extensive subglacial water activity [e.g., Fricker *et al.*, 2007; B. E. Smith *et al.*, 2009; Creyts and Schoof, 2009; Siegfried *et al.*, 2014; Fricker *et al.*, 2016] and by the recognition that basal conditions are of major importance to the proper formulation of numerical simulations of ice sheet evolution in a warming climate [e.g., Nowicki *et al.*, 2013].

Quantification of the thermodynamic state of the WAIS is essential for properly assessing the time scales and amplitudes of potential unstable collapse. Examination of the error and uncertainty caused by relatively poor characterization of the ice sheet thermodynamic and phase states is now under increased scrutiny, as any assessment of how future ice flow might change is related to the heat flux condition applied at the solid Earth-ice interface [e.g., Rogozhina *et al.*, 2012; Larour *et al.*, 2012a]. A zeroth-order problem is to attack the uncertainty in background heat flux at the bed.

Snow falling on an ice sheet provides continuous replenishment of a thick thermally insulating layer. As the ice temperature melting point decreases with pressure, the thicker the ice sheet, the easier it is for the geothermal heat flux to raise the basal temperature to the melting point. The sensitivity of basal melt to geothermal

heat flux,  $q_{\text{GHF}}$ , is revealed by the theory of *Budd et al.* [1984] for one-dimensional flow lines. It emphasizes the linear relation between basal temperature and geothermal flux and predicts the presence of basal meltwater beneath most of the Antarctic ice sheet for  $q_{\text{GHF}} \geq 80 \text{ mW/m}^2$ . Most numerical models of the polar ice sheets assume the geothermal flux to be  $42 \leq q_{\text{GHF}} \leq 65 \text{ mW/m}^2$  [*Siegert and Dowdeswell*, 1996; *Llubes et al.*, 2006], as pointed out by *Rogozhina et al.* [2012]. However, in West Antarctica, which experiences active Cenozoic volcanism and rift formation, the question of higher  $q_{\text{GHF}}$  is especially important as geothermal heat flux exceeds  $70 \text{ mW/m}^2$  in analogue regions, such as the continental United States, west of the Rocky Mountain Ranges [*Ramirez et al.*, 2016; *Davies*, 2013; *Blackwell*, 1989].

*Pattyn* [2010] has shown that more than half of the Antarctic ice sheet base reaches the pressure melting point and estimates the total continent-wide basal meltwater production rate to be about  $65 \text{ Gt/yr}$ . Such a production rate is substantial, amounting to roughly 3% of the surface accumulation rate in Antarctica. Using lakes as an indicator of the presence of basal meltwater, similar to what was done by *Siegert and Dowdeswell* [1996], the analysis of *Pattyn* [2010] derived a modified geothermal heat flux map connected to the observations of Antarctic basal water conditions. However, this map lacks any new solid Earth information that can now be derived from the large-scale broadband seismic stations that are currently imaging the mantle and crustal environment [e.g., *Chaput et al.*, 2014; *Emry et al.*, 2015; *Lloyd et al.*, 2015; *Heeszel et al.*, 2016]. The three-dimensional (3-D) seismic wave velocity structure derived from this new data provides new constraints on tectonic conditions under the ice sheet. Any ice sheet observation that confirms the presence of mantle plume conditions has profound implications for regional mantle properties beneath the WAIS. Mantle viscosity is exponentially temperature dependent, and the viscous response time to loading and unloading by ice is, also, governed by an exponential dependency on the viscosity. A hotter mantle, therefore, predicts drastically reduced time scales over which glacial isostatic adjustment stress relaxation occurs [e.g., *Ivins et al.*, 2000].

The hypothesis of a deep mantle plume of sufficient heat transport to manifest Cretaceous to Holocene age volcanism and present-day seismicity in West Antarctica dates to the 1980s. However, no seismic imaging provided support for a plume beneath Antarctica until surface wave mapping by *Sieminski et al.* [2003] and *Montelli et al.* [2006] mapped a slow structure in the top of the lower mantle beneath the western Ross Sea.

Central to the 3 km MBL uplift is a dome that contains 18 major high-standing volcanoes of felsic alkaline and alkali basaltic chemistry. The majority of these volcanoes form linear chains that age toward the center of the province [*Storey et al.*, 2013]. Late Cenozoic volcanism (28–35 Ma) may well be associated with a single active plume [*LeMasurier and Rex*, 1989; *LeMasurier and Landis*, 1996]. Alternatively, a longer-lived and more broadly scaled mantle upwelling may have arrived to the lithospheric environment circa 100 Ma, with analysis of uranium and lead isotopic ratios supporting a separation from slab material that stagnated at the top of the lower mantle beneath Gondwana [*Steinberger*, 2000; *Panter et al.*, 2006; *Sutherland et al.*, 2010; *Spasojevic et al.*, 2010].

Global seismic tomography, having inherently lower resolution, seems to support the broad-scale, longer-lived model, while more recent high-resolution tomography resulting from the broadband seismic Antarctic Polar Earth Observing Network seems to support the single, younger, and more spatially focused model [e.g., *Hansen et al.*, 2014; *Accardo et al.*, 2014; *An et al.*, 2015; *Emry et al.*, 2015; *Lloyd et al.*, 2015; *Heeszel et al.*, 2016]. The seismic images reveal the pattern and amplitude of upper mantle anisotropy as well as lateral variability in shear and compressional wave velocity and, collectively, lend support for the hypothesis of a lower mantle plume origin as the cause of the more youthful MBL volcanism and geophysical structure. Compelling evidence of ongoing magmatic movement at lower crustal depths has been found recently in long-period earthquakes [*Lough et al.*, 2013], and these events indicate that the locus of activity has moved  $\sim 55 \text{ km}$  southward of the Quaternary eruptions of Mount Waesche in the Executive Committee Range (ECR, see Figure 1). The surface manifestations of continental plumes are approachable using simple models when the lithospheric plate has been nearly stationary over the past 30 Ma, as is the case with Antarctica [e.g., *Gripp and Gordon*, 2002]. As a consequence, we may be able to further test the hypothesis of a single-focused plume by modeling its thermal interaction with the base of the ice sheet.

In this study, we conduct numerical modeling for simulating the interaction between the solid Earth mantle plume and the ice sheet thermal structure. While our focus is primarily on the MBL dome, it is also instructive to perform computations for an area around Subglacial Lake Whillans (SLW) where there is abundant

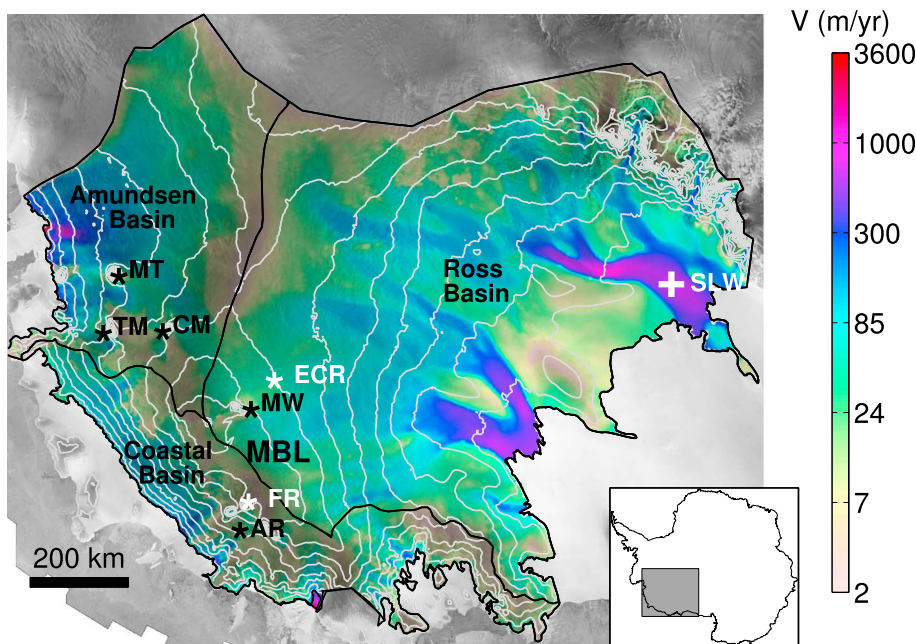


**Figure 1.** Modeled ice surface velocities overlaid on a Moderate Resolution Imaging Spectroradiometer Mosaic of Antarctica. Locations mark Marie Byrd Land (MBL), Ames Range (AR), Crary Mountains (CM), Executive Committee Range (ECR), Flood Range (FR), Mount Takahe (MT), Mount Waesche (MW), Toney Mountains (TM), and the Whillans Ice Stream Subglacial Access Research Drilling project drilling site (SLW). Black lines delineate the contour of the model domain and the three main basins: the Amundsen Basin, the Ross Basin, and the Coastal Basin. Grey lines indicate ice surface elevation every 250 m. Stars indicate active volcanoes, and white symbols represent the three locations where the plume experiments with varying mantle plume parameters (Plume FR, Plume ECR, and Plume SLW; see Table 1) are performed.

evidence for basal water. Observations in both regions suggest the presence of magmatic activity and high geothermal flux. While there are measurements of geothermal heat flux near mantle plumes, these suffer from their spatial sparsity, often faced with difficult logistics in the deep ocean [e.g., Nyblade and Robinson, 1994]. Harris and McNutt [2007] show that there are significant sampling deficiencies in ocean floor heat flow studies that have targeted hotspots. These owe to the lack of sufficient spatial density combined with a heterogeneous fluid convective transport through the shallow crust. Studies at La Réunion [e.g., Bonneville *et al.*, 1997] and Hawaii hotspot tracks, where spatial sampling is highest, tend, however, to show that the anomaly with respect to a background plate model is small, about  $10 \text{ mW/m}^2$ . Jaupart *et al.* [2015] conclude that the heat supplied by the mantle plume hotspot in the oceanic lithospheric environment is suppressed by the fact that it locks deeply to the base of the lithosphere. Studies of continental flux where rising plumes meet a rheologically weaker lithosphere than beneath the ocean plates [e.g., Kohlstedt *et al.*, 1995] reveal anomalies that are an order of magnitude larger. The most widely studied and data-rich example is the Yellowstone hotspot. We therefore use an analytical mantle plume model parameterization that is capable of producing realistic spatial patterns of geothermal heat flux where observations are in abundance [e.g., DeNosaquo *et al.*, 2009]. A complete discussion of the parameterization is presented in Appendices A–C.

The thermal regime of the 3-D ice flow model is based on the enthalpy framework, an energy-conserving formulation that allows modeling cold and temperate ice [Aschwanden *et al.*, 2012], and includes thermal advection, diffusion, deformational heat, and basal heat flux. The location and extent of the mantle plume beneath the WAIS is only roughly inferred from seismic data. We therefore perform here a series of numerical experiments with varying plume location and intensity to characterize mantle plume-related basal conditions in MBL and beneath the WAIS. We first summarize evidence supporting the presence of a mantle plume in West Antarctica and validation of the mantle plume parameterization. We then detail the ice sheet model as well as the experiments performed. We finally present and discuss our results and their implications for the presence of a mantle plume in West Antarctica.

## 2. Geological and Geophysical Data Supporting a Youthful Plume in MBL

### 2.1. Geochemical and Geodynamic Setting

A detailed analysis of the potassium-argon dating of late Cenozoic West Antarctica volcanism by *LeMasurier and Rex* [1989] revealed that the alkaline basaltic basement rocks beneath MBL and spatiotemporal volcanism patterns of the past 18 Ma have a mantle origin. The petrology of the magmas associated with the basement suggests that a mantle plume rose to reach the base of the lithosphere at about 28–30 Ma, consistent in dimension with the Yellowstone hotspot in the western United States [*LeMasurier and Landis*, 1996; *Winberry and Anandakrishnan*, 2004; *LeMasurier*, 2008]. *Husson and Conrad* [2012] studied mantle flow capable of either promoting or suppressing active plume volcanism and determined that the regional tectonic setting is not incompatible with an active mantle plume. This mantle hotspot interaction with the crust/lithosphere of this geological province was preceded 55 Ma earlier by a larger plume event associated with a major continental breakup [*LeMasurier*, 2008; *Storey et al.*, 2013].

### 2.2. Geophysical Inferences From Seismic Data

Analysis of Rayleigh wave paths that cross Antarctica reveals low-velocity structures that have been interpreted to support the MBL hotspot hypothesis [*Sieminski et al.*, 2003]. Over the past 15 years, the cumulative number of ray paths has allowed much higher resolution for seismic imaging of the upper mantle structure beneath Antarctica and doubled the resolving capability. Figure 2b shows the mantle shear velocity structure from regional Rayleigh wave tomography at 130 km depth, showing a low-velocity region indicating a large thermal anomaly centered beneath MBL [*Heeszel et al.*, 2016]. Regional body wave tomographic images also show a low-velocity anomaly at 100–400 km depth [*Lloyd et al.*, 2015], and seismic anisotropy measurements from shear wave splitting show a radial pattern of fast axis directions that is interpreted as flow from a mantle plume [*Accardo et al.*, 2014]. Large-scale body wave tomography [*Hansen et al.*, 2014] shows low velocities continuing into the transition zone. This, along with receiver function images showing a thin transition zone beneath the Ruppert Coast area of the MBL dome [*Emry et al.*, 2015], suggests that a plume source may not go directly into the lower mantle but may instead be tilted. The P wave imaging conducted by *Hansen et al.* [2014] shown in Figure 2c reveals a similar continuous feature. The seismic data are therefore consistent with a mantle plume under MBL that originates in the transition zone or deeper in the lower mantle.

Growth of the structural volcanic and dynamic uplift in MBL was initiated between 29 and 25 Ma [*LeMasurier*, 2006], a time after relative motions between East and West Antarctica have greatly diminished and the relatively stable convergent continental boundary has been established after about 50 Ma [*Eagles et al.*, 2004; *Torsvik et al.*, 2008]. Plume theory is consistent with an instability at an unstable thermal boundary layer below the 660 km mantle seismic transition zone that could be formed at, or before, 50 Ma and arrive at the crust 20 Ma later.

### 2.3. Geothermal Heat Flux at the Base of the Antarctic Ice Sheet

Few direct observations of geothermal flux over mantle plumes exist. Using existing mantle plume data sets as boundary conditions at the base of the Antarctic ice sheet would therefore not allow performing simulations sampling a large spectrum of geothermal heat flux conditions with plume of varying intensity. We therefore rely on a mantle plume parameterization that includes both the deep temperature driving the plume and the buoyancy flux Rayleigh number (see Appendices A–C for more details on the analytical mantle plume description). This simple parameterization does not allow reproducing details of plume growth or plume heads, but it enables us to span the range of observed geothermal heat flux for plumes at the surface of the Earth, and a broad range of examples are included in the supporting information. Our parameterization of the plume uses the concept of a Nusselt number ( $\varepsilon$ ). In thermally buoyant fluid dynamics this is just the ratio of mean vertical advective heat flux and conductive heat flux in the state of nonfluid motion to the conductive heat flux in the state of nonfluid motion [see *Howard*, 1963, p. 410, equation (10)]. It is the essence of many simplifications (or parameterizations, one important example being the “parameterized convection” used in comparative planetology) throughout geophysical fluid dynamics wherein thermal coupling is involved [e.g., *Holland and Jenkins*, 1999, see also *Turner*, 1973, chap. 7]. In the top boundary layer of a convective system, vertical advection is very small, and essentially, all the transport becomes conductive. We use an approximation such that transport across a top layer is mimicked by increasing the effective thermal conductivity within a cavity that we define as the spatial domain of our idealized mantle plume. Such an approximation also allows the heat transport to be kept mainly within the spatial domain of this cavity.

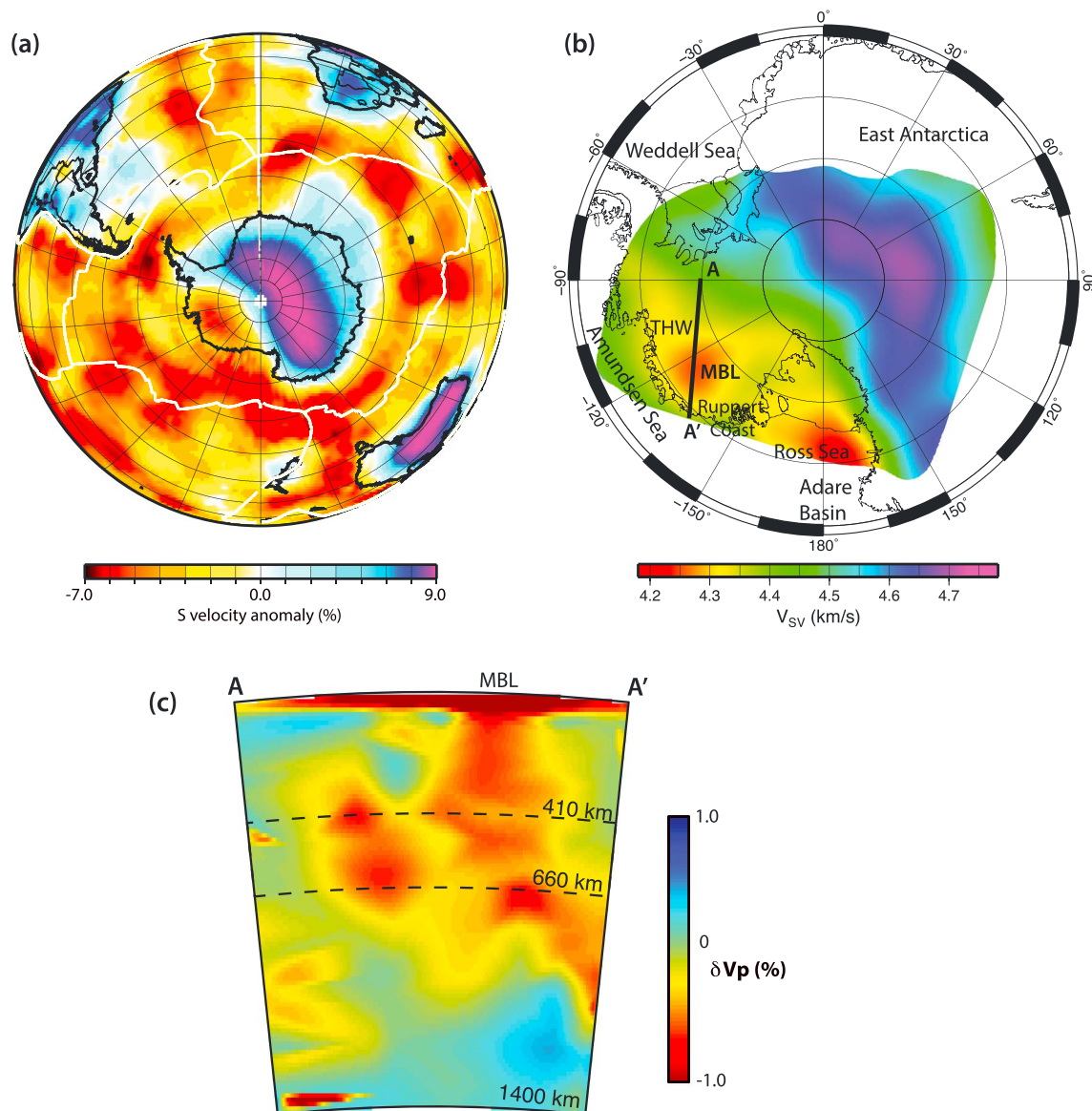


**Figure 2.** (a) Map of  $S$  velocity at 150 km depth from *Shapiro and Ritzwoller* [2002] and (b) map of  $S$  wave velocity at 130 km depth in Antarctica from regional Rayleigh wave phase velocity inversion [*Heeszel et al.*, 2016].  $V_{SV}$  is the velocity of the vertical component of the seismic shear wave [see *Aki and Richards*, 1980, p. 100]. (c) Mantle cross section through the tomographic  $P$  wave model of *Hansen et al.* [2014] along profile A-A'. Other profiles are shown in *Hansen et al.* [2014]. Acronyms refer to Thwaites Glacier (THW) and Marie Byrd Land (MBL).

#### 2.4. Plume Calibration and Quantification

As discussed above, precise measurements of plume heat flux are elusive and there are limited cases to calibrate the characteristics of the parameterization. One notable exception is the Yellowstone area, where geothermal heat flux has been extensively studied [*DeNosaquo et al.*, 2009; *B. E. Smith et al.*, 2009] and measurements are sufficiently dense [*Blackwell et al.*, 2007].

In order to validate our analytical plume model, we used observations of the Yellowstone area reported in *DeNosaquo et al.* [2009] (see Figure 3). The analytical plume model of the Yellowstone area has a 150 km radius [*B. E. Smith et al.*, 2009], the modeled plume head depth is 7 km in order to account for the upper crustal magma reservoir [*Huang et al.*, 2015], and the Nusselt number is equal to 8 [*B. E. Smith et al.*, 2009]. This Nusselt number,  $\epsilon$ , approximates the advective heat transport by increasing the thermal conductivity in the plume conduit (see Appendix B). The rocks interior to the space occupied by the plume then have, in essence, a mock model thermal conductivity, as this provides a convenient mathematical vehicle to modulate the

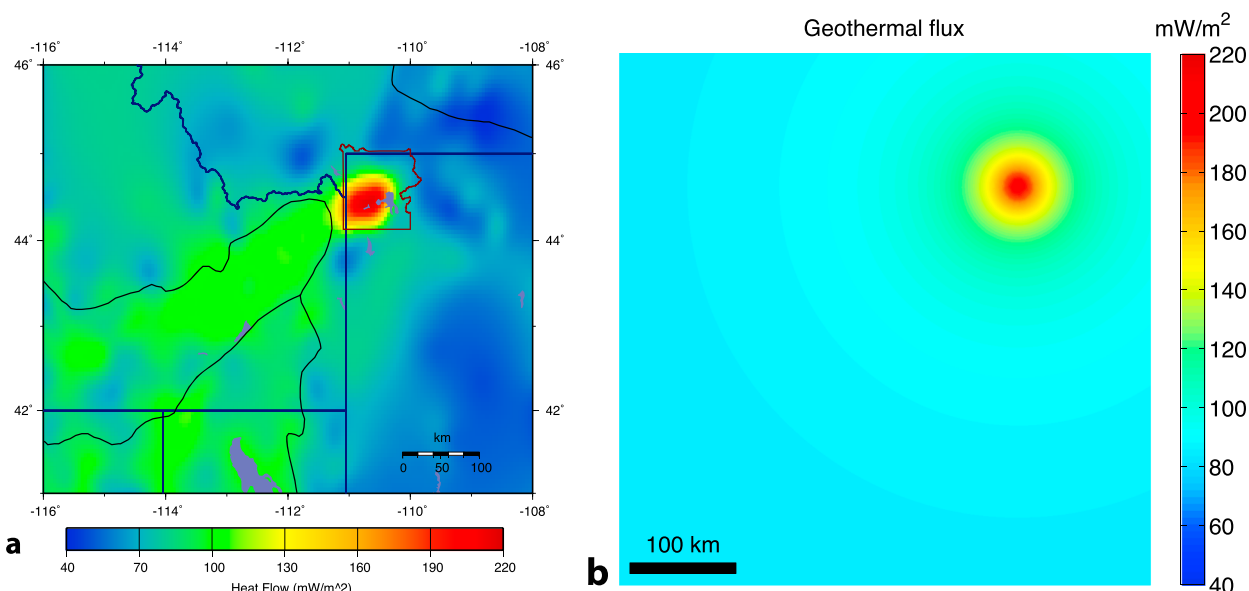


**Figure 3.** (a) Observed [DeNosaquo *et al.*, 2009] and (b) modeled geothermal heat flux (in  $\text{mW}/\text{m}^2$ ) of the Yellowstone area. The 100 km scales are shown on both figures.

vertical heat transport associated with advection. We do not advocate that this is a good model for examining any other thermally related properties of mantle lithosphere, yet it quite adequately represents the geometry and vertical transport with respect to the bottom of the ice sheet and its interior that we focus on using the full-Stokes thermomechanical ice sheet modeling. The plume origin is uncertain, but tomography images low-velocity mantle for at least 900 km depth [Schmandt *et al.*, 2012], so we assume the origin of the plume to be at 2300 km depth, within a thermal boundary layer just above the post-perovskite transition depth. The modeled crust is 47 km, with the upper crust being 14 km thick [Huang *et al.*, 2015], while the crustal heat is chosen identical to default parameters in Table C1.

While the model may have somewhat arbitrary geometrical characteristics, it serves our unique purpose well. The analytical plume model captures the most important large-scale features of the geothermal surface expression, with a heat flux of about 200  $\text{mW}/\text{m}^2$  in a radius of about 40 km above the plume, sharply decreasing to less than 100  $\text{mW}/\text{m}^2$  over a distance of 100 km. This simple model does not allow reproducing the highest geothermal flux up to 2000  $\text{mW}/\text{m}^2$  measured on the Yellowstone Plateau [B. E. Smith *et al.*, 2009; DeNosaquo *et al.*, 2009]. However, we do not explicitly model the magmatic transport of heat that involves a liquid phase, something that affects heat flux at the center of the these elevated values and is caused by hydrothermal fluid circulation [Huang *et al.*, 2015].

Plume and hotspot intercomparisons employ some standard measures [Courtillot *et al.*, 2003; King and Adam, 2014], and it is most appropriate to provide theoretically consistent quantifications. Sleep [1990] offered several ways to observationally approach quantitative intercomparisons. One technique is to use the geoid and topographic swell to compute the buoyancy flux,  $B_{\text{plume}}$ , and by integration over the area, a corresponding heat transport,  $Q_{\text{plume}}$ , may also be estimated (see equations (A9) and (A10)). This method calibrates plume strength, something that requires accounting for the lateral advection caused by plate motion, plume head evolution, and shear. Our parameterized plume of similar central heat flux, but lacking plate-induced lateral thermal advection of mantle material (corresponding to our MBL case) predicts a buoyancy flux,  $B_{\text{plume}} \approx 0.10 \text{ Mg/s}$  for the Yellowstone area, somewhat lower than the 0.25 Mg/s estimate reported in R. B. Smith *et al.* [2009], while predicting  $Q_{\text{plume}} \approx 4.06 \text{ GW}$ , close to the value of 5.0 GW given by R. B. Smith *et al.* [2009] and Jaupart *et al.* [2015].

More precise estimates of  $B_{\text{plume}}$  for MBL would require estimating the ice flow enhanced sediment erosion and obtaining an improved understanding of the subtle plate motions above the plume over at least the

**Table 1.** List of Experiments<sup>a</sup>

Experiments	$q_{\text{GHF}}$ Source	Plume Location	Plume Depth <sup>b</sup> (km)	Plume Radius (km)	$\varepsilon^c$	Max. $q_{\text{GHF}}$ (mW/m <sup>2</sup> )	$Q_{\text{plume}}^d$ (TW)
Initialization	SR04 <sup>e</sup>	NA	NA	NA	NA	NA	NA
No plume	60 mW/m <sup>2</sup>	NA	NA	NA	NA	NA	NA
Plume FR	Plume parameter	FR	20–40	50–200	3–3000	60–200	0.002–0.42
Plume ECR	Plume parameter	ECR	20–40	50–200	3–3000	60–200	0.002–0.42
Plume SLW	Plume parameter	SLW	20–40	50–200	3–3000	60–200	0.002–0.42
Plume A	Plume parameter	Varying	30	200	30	128	0.003
Plume B	Plume parameter	Varying	20	100	3000	180	0.11
Plume C	Plume parameter	Varying	0	100	3000	258	0.11

<sup>a</sup>NA, not applicable.<sup>b</sup>Plume depth refers to the top of the plume depth below the crust.<sup>c</sup> $\varepsilon$  is a proxy for the Nusselt number (see section 2.4).<sup>d</sup> $Q_{\text{plume}}$  was computed based on the equations in Yoshida [2012].<sup>e</sup>SR04: Shapiro and Ritzwoller [2004].

past 30 Ma. We calculate values for  $B_{\text{plume}}$  and  $Q_{\text{plume}}$  using the integrals over a circular area surrounding the plume axis [see Yoshida, 2012] from our analytical model around the center of the vertical swell that do not include these two effects.

### 3. Ice Sheet Modeling

Numerical modeling of ice flow and heat transport is used to evaluate the impact of the presence of a mantle plume on the WAIS. The study is, essentially, aimed at providing fundamental quantification of the main question posed by Blankenship *et al.* [1993]: What is the relative stability of the ice sheet when underlain by an active hotspot?

While our study focuses on the environs of MBL, we also seek to determine if heat from a mantle plume is compatible with the observational constraints for the entire base, volume, and surface of WAIS. We rely on the Ice Sheet System Model (ISSM) [Larour *et al.*, 2012b], with formal incorporation of the analytical mantle plume model (equation (B8)), for performing a set of experiments listed in Table 1 that address the question of plume compatibility with available observations. Default parameters are listed in Table C1 and used for all the experiments except if stated otherwise in the text. The model is set up to reproduce the details of the known ice velocity field of WAIS as mapped from space (see Figure 1).

#### 3.1. Numerical Experiments

We perform a number of experiments with different plume locations and parameters. These parameters are designed to reproduce the range of uncertainties associated with mantle properties and plume locations.

##### 3.1.1. No-Plume Case

An initial run with a spatially homogeneous geothermal flux generated by crustal radiogenic heat production and lithospheric heating is performed as a nominal case for comparison with the other simulations (see Figure 4). In the absence of a mantle plume, with a lithosphere of about 80 km, the heat produced is about 60 mW/m<sup>2</sup> [Heeszel *et al.*, 2016]. Proxy methods have been used to estimate basal heat flux in Antarctica, and Maule *et al.* [2005] suggest a total heat flux of 55 to 65 mW/m<sup>2</sup> in West Antarctica, so we use a uniform basal heat flux of 60 mW/m<sup>2</sup> for the no plume case (see Table 1). Such a value is consistent with the recent estimate by Ramirez *et al.* [2016] for the broader West Antarctic Rift System, a region potentially influenced by the spreading of the mantle plume head (see Figure 2c).

##### 3.1.2. Plume Locations

We first simulate a mantle plume under Flood Range (FR) in MBL (Figures 1 and 2), as seismic observations suggest the presence of a regional hotspot of late Cenozoic age [Lloyd *et al.*, 2015]. The second location chosen for the plume is 55 km south of ECR, as measurements of seismic activity suggest the presence of uppermost mantle and lower crustal magmatic activity [Lough and *et al.*, 2013]. The third location we investigate is set under SLW (Figure 1), where there is little evidence of a deep-seated plume but there is evidence of warmer than average mantle at asthenospheric depth [Heeszel *et al.*, 2016]. While few direct estimates of geothermal

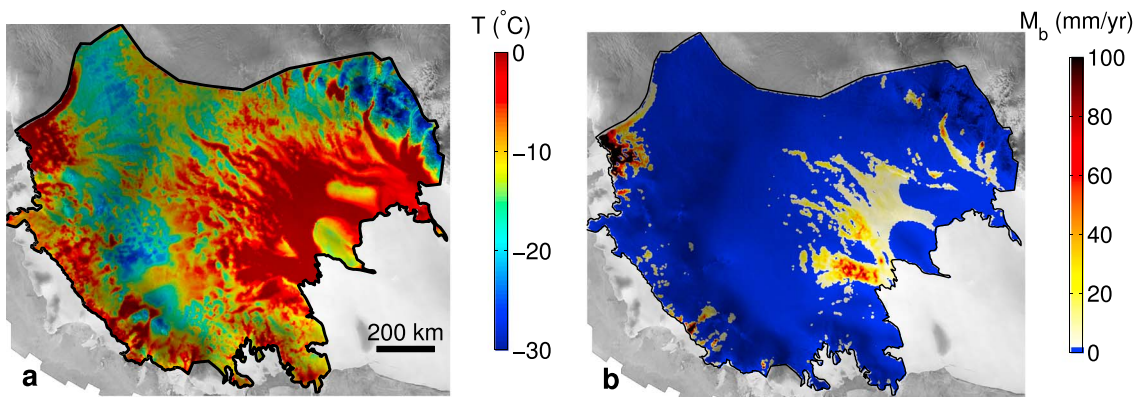


**Figure 4.** Basal conditions for the no-plume case. The geothermal flux is homogeneous and equal to  $60 \text{ mW/m}^2$ . (a) Modeled pressure-corrected basal temperature ( $^\circ\text{C}$ ). (b) Modeled basal melting rate ( $\text{mm/yr}$ ).

flux exist under the Antarctic Ice Sheet (AIS), the Whillans Ice Stream Subglacial Access Research Drilling (WISSARD) project [Fisher *et al.*, 2015] has provided the first direct observations of geothermal flux,  $q_{\text{GHF}}$ . This area was chosen as the drill site because the presence of numerous lakes detected from satellite laser altimetry [Fricker *et al.*, 2007; Fricker and Scambos, 2009] suggests an important amount of basal meltwater caused by elevated geothermal heat flux in this area. The  $q_{\text{GHF}}$  was measured in rock sediments deposited in the substructure of SLW, and below almost 800 m of ice. The values estimated are very high by continental standards, reaching  $285 \text{ mW/m}^2$ . The estimates are based on the measured thermal gradient and thermal conductivity of the sediments under the ice and lake water. The WISSARD experiment measured a value of  $q_{\text{GHF}}$  that is significantly larger than values mapped from geophysical inference in this region [Maule *et al.*, 2005; Shapiro and Ritzwoller, 2004].

### 3.1.3. Plume Properties

Physical properties of the mantle plume are relatively poorly constrained, and we therefore perform a sensitivity analysis to represent the range of uncertainty in the main parameters for these three sets of experiments (Plume FR, Plume ECR, and Plume SLW; see Table 1). In our simulations, all the plumes have lower mantle origin at 2300 km below the Earth's surface, approximately at the top of a boundary layer above post-perovskite transition zone [Maxwell *et al.*, 2015]. Moving its origin to the base of the mantle changes the geothermal heat flux by less than 3% and has a negligible impact on the basal water production. Parameters used for mantle plume properties are as follows: our proxy Nusselt number,  $\epsilon$  (see Appendix B), is equal to 3, 30, 300, or 3000; the plume radius,  $c$ , to 50, 100, 150 or 200 km; and the plume depth below base of the crust,  $D$ , to 20, 30 or 40 km (see Appendix C and Figure C1). The combination of these parameters results in 48 simulations, which are performed for each of the three locations (FR, ECR, and SLW). Modeled geothermal heat flux produced at the base of the ice sheet directly above the plume therefore ranges between  $60$  and  $200 \text{ mW/m}^2$ , while the total heat advected by the mantle plume ranges from 0.005 to 0.42 TW, and the buoyancy flux ranges between 0.09 and 9.3 Mg/s, consistent with estimated values for other mantle plume locations [Sleep, 1990; Yoshida, 2012; Jaupart *et al.*, 2015].

### 3.1.4. Uncertainty in Plume Location

One of our objectives is to determine areas where the presence of a mantle plume is compatible with the AIS as we know it. For this reason, we simulate the impact of several mantle plumes of varying intensity for multiple locations in our model domain. We first investigate the effect of a weak plume, Plume A (see Table 1), creating a geothermal heat flux of  $q_{\text{GHF}}^{(0)} = 128 \text{ mW/m}^2$  at the base of the ice sheet directly above the plume location, a total heat flow transport,  $Q_{\text{plume}}$ , of about 3 GW, and a buoyancy flux  $B_{\text{plume}}$  of 0.18 Mg/s. In this case, plume parameters are  $c = 200 \text{ km}$ ,  $D = 20 \text{ km}$ , and  $\epsilon = 30$ . In order to assess the impact of the weak plume on basal conditions, we vary its location by increments of 50 km along both horizontal directions, which yields a total of 540 independent simulations.

We then characterize the impact of two large thermal transport enhancements, called Plume B and Plume C (see also Table 1), both with  $\epsilon = 3000$  and  $c = 100 \text{ km}$ , creating a total heat flow transport,  $Q_{\text{plume}}$ , of about 0.11 TW and a buoyancy flux  $B_{\text{plume}}$  of 2.3 Mg/s. Plume B and Plume C have  $D = 20 \text{ km}$  and  $D = 0 \text{ km}$ ,

respectively, and produce a maximum flux  $q_{\text{GHF}}^{(0)} = 180 \text{ mW/m}^2$  and  $q_{\text{GHF}}^{(0)} = 258 \text{ mW/m}^2$  at the base of the ice sheet directly above the plume location. Plume C has a maximum geothermal heat flux of  $258 \text{ mW/m}^2$  in the center of the plume, similar to the value measured by *Fisher et al.* [2015] for SLW and therefore aims to test the impact of large geothermal heat flux in different locations of our model domain. For both Plume B and Plume C, we run simulations at the same locations as Plume A above, which yields a total of 1080 independent simulations.

### 3.2. Model Setup and Data Sets

#### 3.2.1. Domain

The model domain includes a large part of the WAIS, from the five major ice streams feeding the Ross Ice Shelf to Thwaites Glacier. A series of smaller outlet glaciers north of the ECR flowing toward the coastline is also included. The domain extends from the ice sheet divide to the grounding line of each outlet glacier. Floating extensions of the ice streams are not included in our computational domain, as their basal conditions are determined by oceanic circulation and not geothermal heat flux. Figure 1 shows the extent of the modeled domain as well as the location of FR, ECR, and SLW.

The domain is discretized onto 86,365 horizontal triangular elements with a resolution of about 5 km. The horizontal mesh is then extruded into 20 vertical layers, between the bedrock and the ice surface elevation [*Fretwell et al.*, 2013]. Thinner layers are used near the base and thicker layers close to the surface of the ice sheet, the deepest layer being 50% thinner than the surface layer. The variable layer thickness reduces the overall computational effort while robustly capturing the sharp thermal gradient close to the ice/bedrock interface. This results in a mesh of about 1,640,000 prismatic elements. The enthalpy field equation is solved using linear P1 elements, while the stress balance equation is solved using full-Stokes equations and Taylor-Hood elements [*Gresho and Sani*, 2000].

#### 3.2.2. Plume-Ice Equilibrium State

To simulate the thermal state of the ice sheet and its basal conditions, we use an enthalpy formulation [*Aschwanden et al.*, 2012], integrated and validated in ISSM [*Seroussi et al.*, 2013; *Kleiner et al.*, 2015]. The steady state temperature and melting rates at the base of the ice sheet are computed, neglecting changes due to past variations in climatic conditions and their impact on ice sheet flow [*Seroussi et al.*, 2013]. Horizontal and vertical advection, as well as diffusion, internal generation of heat by viscous dissipation, basal heat due to geothermal flux, and frictional heating caused by sliding at the ice-bedrock interface are all included in the model. The mean annual surface temperature from a regional atmospheric climate model, RACMO 2.1 [*Lenaerts et al.*, 2012], is imposed at the surface of the ice sheet. Surface melt and runoff are not considered, as they are negligible in this region of Antarctica [*Lenaerts et al.*, 2016]. *Shapiro and Ritzwoller* [2004] derived a geothermal heat flux map from surface wave mapping of the lithosphere. This map is used in the initialization process of the ice flow model. The geothermal flux maps for all other experiments are derived from the mantle plume and two-layer crustal heat sources once a formal iteration process has converged.

Accurate representation of cold ice advection from the ice sheet interior is critical for correctly capturing the thermal state of the ice sheet. In order to properly include ice motion and therefore vertical advection, we use the 3-D full-Stokes equations to compute the stress balance and capture the 3-D motion of the ice. We infer the unknown basal friction to match observed surface velocities using an adjoint-based inversion, similar to those described by *MacAyeal* [1989] and *Morlighem et al.* [2010]. The cost function employed for inversions includes logarithmic and absolute terms, capturing surface velocity features of both slow- and fast-flowing regimes, as well as a Tikhonov regularization term [*Morlighem et al.*, 2010; *Seroussi et al.*, 2014]. We exploit the continental-scale, horizontal surface velocity field of *Rignot et al.* [2011] to guide both the inverse problem and the inflow boundary conditions. A viscous sliding law is used at the base of the ice sheet similar to *Seroussi et al.* [2013]. Ice velocity normal to the bedrock is set equal to the basal melt rate to avoid either false cavitation or penetration into the bedrock. The upper boundary condition on the ice is maintained as stress free, as the atmospheric pressure is negligible. Temperate ice that includes a positive water fraction is significantly softer than cold ice [*Duval*, 1977], so we rely on a composite rheological law that is sensitive to both ice temperature and water fraction [*Lliboutry and Duval*, 1985].

The momentum balance and thermal equations form a fully coupled system, as changes in ice temperature impact the effective ice viscosity, while changes in ice velocity impact the temperature and heat distribution through advection and deformational heat. This coupled system is computed until a thermomechanical

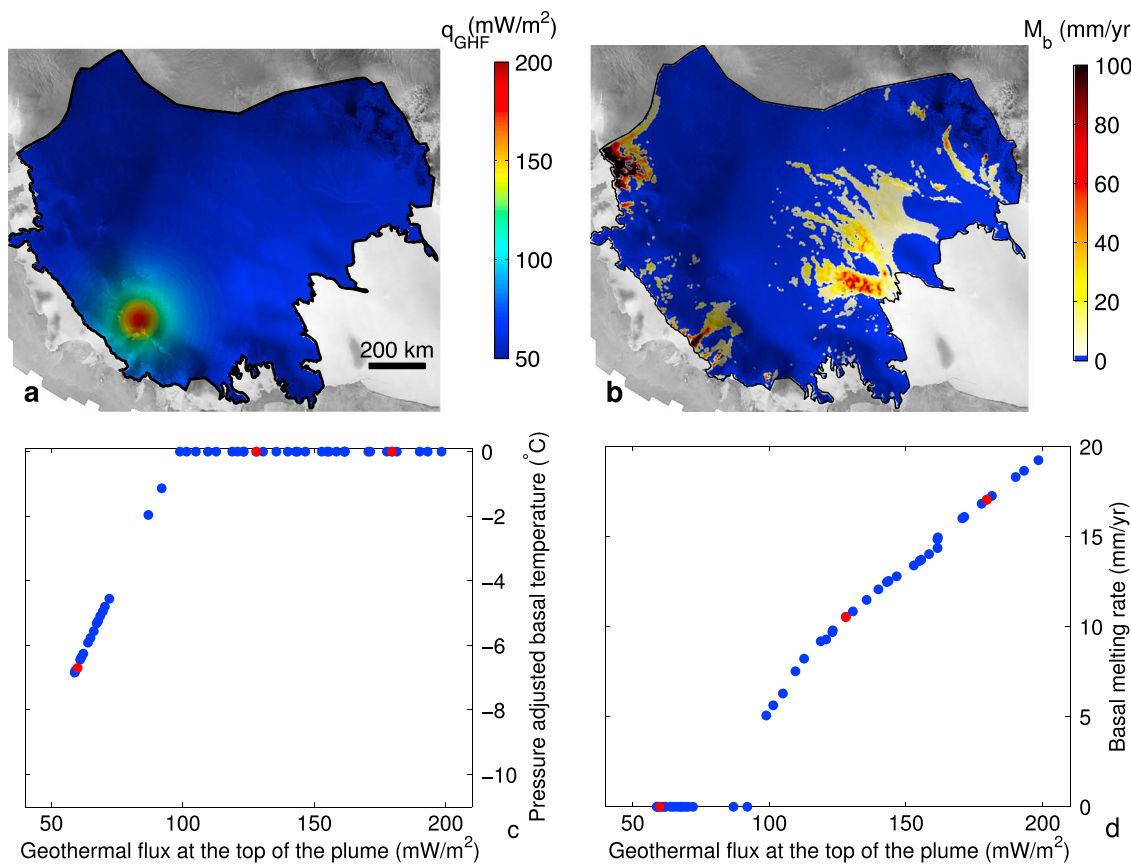


**Figure 5.** Basal conditions for the 48 Plume FR experiments, with a plume centered beneath the Flood Range along the Ruppert Coast. (a) Map of heat supplied by the solid Earth with plume characteristics similar to Plume B experiments. (b) Corresponding prediction of basal melting rate (mm/yr). (c) Predicted pressure-adjusted basal temperature,  $T_b^{(0)}$ , at the base of the ice sheet directly above the plume as a function of the geothermal flux,  $q_{\text{GHF}}^{(0)}$ , above the plume. (d) Corresponding predicted basal melting rate,  $m_b^{(0)}$ , at the base of the ice sheet directly above the plume. Red dots in Figures 5c and 5d correspond to the no-plume case (60 mW/m<sup>2</sup>) as well as mantle plume experiments with Plume A (128 mW/m<sup>2</sup>) and Plume B (180 mW/m<sup>2</sup>) characteristics.

steady state solution is reached for each iteration of the inverse problem, as in the procedure described by Morlighem *et al.* [2010] and Seroussi *et al.* [2013].

In all the simulations performed, our goal is to determine a steady state temperature, thus computing the impact of differing geothermal flux assumptions on the phase state and temperature of the ice sheet. The potential ramifications of each computed steady state temperature on either the stress balance or the ice stiffness are not explored as a solution property, for they are inherently tied to the use of surface velocity observations as a data assimilating component to formulate the solutions.

#### 4. Impact of Mantle Plume on Basal Conditions

##### 4.1. Nominal Case: No Plume

In the absence of a mantle plume, we consider a geothermal flux generated by the lithosphere and radiogenic heat from the continental crust that is homogeneous and equal to 60 mW/m<sup>2</sup>. Temperature and melting rate simulated for this case are shown in Figures 4a and 4b, respectively. Our simulations reveal that the domain is dominated by a cold base and essentially lacks basal melting. Basal temperatures are coldest at the ice divides and generally increase as ice flows downstream. The predicted patterns owe to both intrinsic heating (bottom frictional heating and viscous dissipation) and geothermal flux heating. Thwaites Glacier and the ice streams feeding Ross Ice Shelf have a temperate base, and predicted melting rates are between a few millimeters per year for Bindschadler and MacAyeal Ice Streams and up to 90 mm/yr for the lower part of Thwaites Glacier, just above the grounding line. The rate of basal meltwater production, integrated over the entire domain, is ~3.24 Gt/yr, of which ~1.85 Gt/yr exits through the Amundsen Sea Sector.

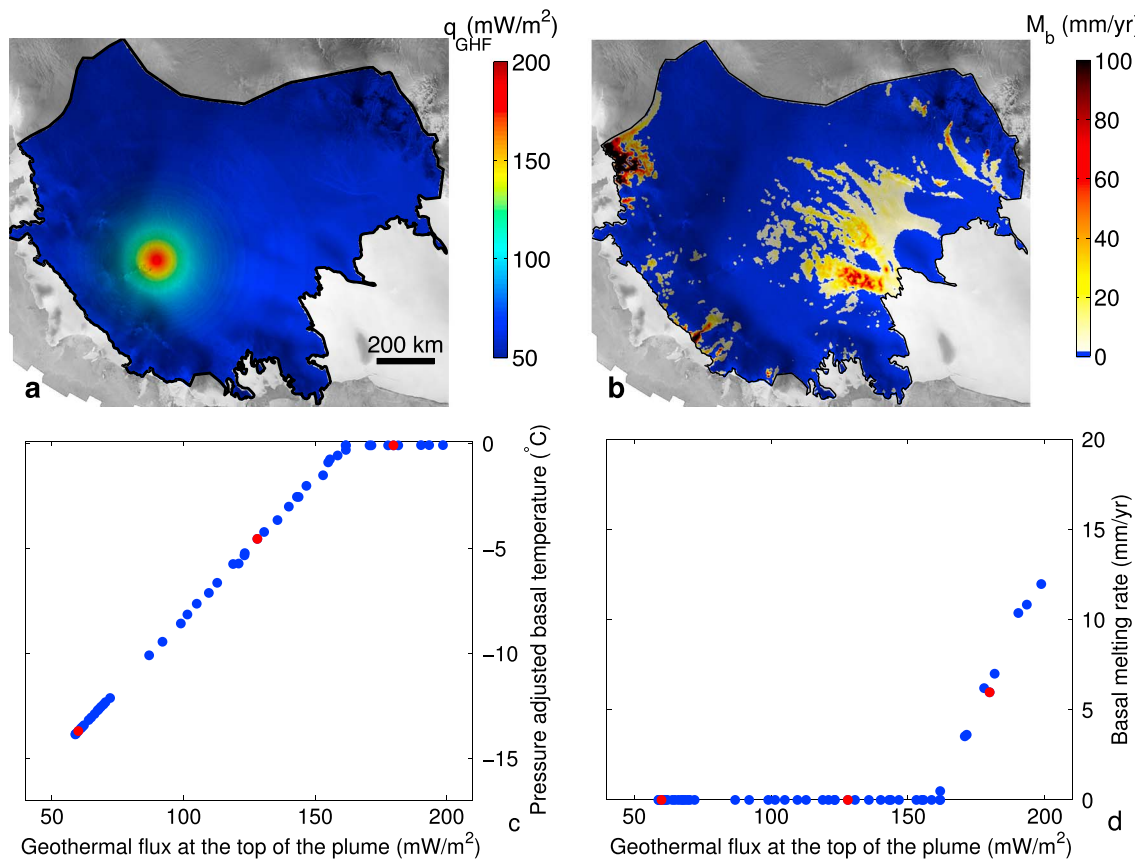


**Figure 6.** Same as Figure 5 but for Plume ECR experiments, with a plume located inland, beneath the Executive Committee Range.

#### 4.2. Hotspot at MBL: Coastal Versus Inland Locations

Figures 5 and 6 summarize the predictions of basal thermal state, when hotspot centers are located either in a more coastal position or in the zone of the central inland domal uplift, respectively, Plume FR and Plume ECR locations, where current low-level seismicity suggests magmatic activity. In order to examine the influence of the robustness of the plume heat transport, we vary the hotspot Nusselt number, plume radius, and the position of the center top of the plume head across a range of parameters (see Table 1) and record the predicted melting temperatures and melt rates computed by ISSM at the ice-solid Earth interface.

In the no-plume case experiment, the geothermal flux is uniform and equal to 60 mW/m<sup>2</sup>. In experiments that include a mantle plume, the geothermal flux at the ice sheet base is increased to at least 76 mW/m<sup>2</sup> away from the plume (see Table 1). This is consistent with the analytical model having the capacity to both simulate the advection of heat from great mantle depths and allowing lateral and vertical diffusion in the mantle and crust. The pattern of predicted basal melting (Figures 5b and 6b) is similar to the case where the lithosphere does not have any plume (Figure 4b). Some areas have basal melt rates that are increased by about 2 to 5 mm/yr, however. Figures 5c and 5d, and 6c and 6d show the pressure adjusted basal temperature,  $T_b^{(0)}$ , and basal melting rate,  $\dot{m}_b^{(0)}$ , directly above the plume for experiments Plume FR and Plume ECR, respectively.

When geothermal heat flux is primarily generated within the crust, ice in FR remains frozen and  $T_b^{(0)} = -6.6^\circ\text{C}$ . For a plume intensity similar to Plume B experiments, ice temperature reaches the pressure melting point and  $\dot{m}_b^{(0)} = 17 \text{ mm/yr}$ . The ice base remains frozen for  $q_{\text{GHF}}^{(0)} \leq 100 \text{ mW/m}^2$  and above this value, melting is predicted at the base of the ice sheet. The basal melting rate,  $\dot{m}_b^{(0)}$ , increases linearly with flux,  $q_{\text{GHF}}^{(0)}$ , and reaches 19 mm/yr for the maximum flux of 198 mW/m<sup>2</sup> in this set of experiments. Above the bedrock of the ECR, ice is colder, and the pressure-adjusted temperature is  $T_b^{(0)} = -13.2^\circ\text{C}$  for our no-plume simulation. The ice remains frozen until  $q_{\text{GHF}}^{(0)} = 160 \text{ mW/m}^2$  and therefore is frozen for Plume A experiment. Basal melt rates in ECR are 6.2 mm/yr for a mantle plume similar to Plume B and 12 mm/yr for the plume generating the highest  $q_{\text{GHF}}^{(0)}$  in this set of experiments. The basal melt rates for many cases computed here seem sustainable and

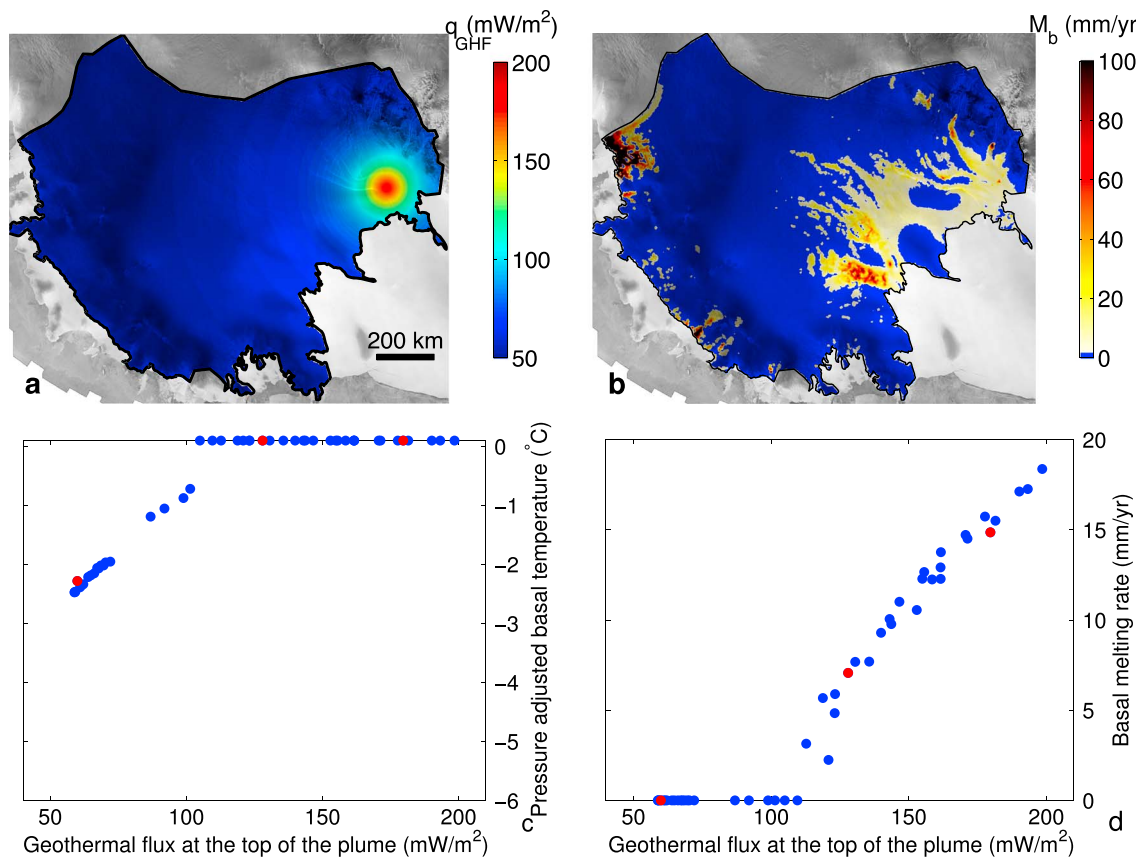


**Figure 7.** Same as Figure 5 but for Plume SLW experiments, with a plume located beneath subglacial Lake Whillans.

compatible with what we understand about water transport among subglacial lakes. Simulations suggest that the amount of water generated by a plume located in ECR is smaller than for FR.

#### 4.3. Mantle-Derived Heat Near SLW

An anomalously high geothermal heat flux of 285 mW/m<sup>2</sup> was measured in 2013 by the WISSARD project in the sediments at the bottom of SLW [Fisher *et al.*, 2015], suggesting the presence of active extensional tectonics in the area. The negative vertically polarized shear wave velocity,  $V_{\text{SV}}$  [Aki and Richards, 1980], is weaker under SLW than MBL. In this area, there is significant evidence of uppermost mantle slow velocity anomalies in the upper 130 km [Heeszel *et al.*, 2016], but there are no volcanic edifices nearby, and seismic tomography does not show deeper slow velocity zones [Heeszel *et al.*, 2016; Hansen *et al.*, 2014]. This might suggest that the anomaly there is not caused by a mantle plume, but is associated with some other manifestation of upward mobility of hot mantle, possibly including anomalous chemistry and mineralogy, and is likely associated with the presence of a rift consistent with Neogene extension [Granot *et al.*, 2010].

For simplicity, we use the plume model to represent anomalous geothermal flux arriving at the base of the ice sheet at SLW. The patterns of geothermal heat flux simulated for plume SLW experiments are displayed in Figure 7. Experiments are similar to those performed for MBL, except that the heat source is centered under SLW.  $T_b^{(0)}$  is  $-2.3^{\circ}\text{C}$  in the no-plume case. Plume intensities similar to Plume A and Plume B raise the temperature to the pressure melting point and generate a basal melting rate of 6.5 and 15 mm/yr, respectively (see Figures 7a and 7b). These experiments provide a geothermal heat flux lower than measured by Fisher *et al.* [2015]. Figures 7c and 7d show that the ice base above the plume remains frozen for  $q_{\text{GHF}}^{(0)} \leq 110 \text{ mW/m}^2$ . The basal-melting rates reach a quite substantial rate, 19 mm/yr, for the most robust plume considered here. While the melting footprint created by the mantle plume is rather limited in space, the location around SLW seems to have influences farther from the plume center than for the two MBL locations investigated here.

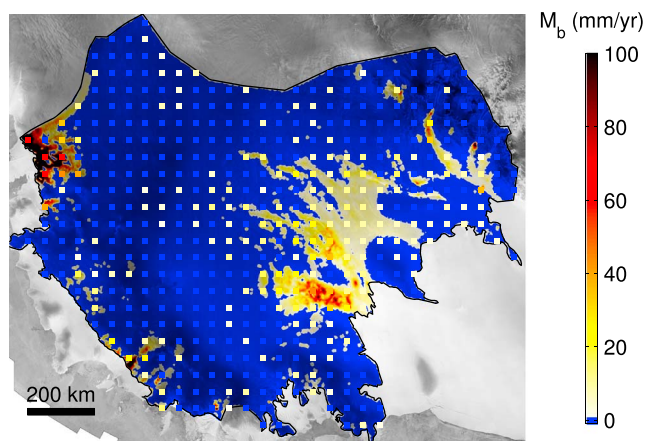


**Figure 8.** Impact of Plume A (weak plume) in different locations. Square color marks the basal melt rate at the base of the ice sheet directly above the center of the plume for each of the 540 independent simulations with different plume locations. Background map is the basal melt rate for the no-plume case.

#### 4.4. Uncertainty in Plume Location

Before seismic imaging from the broadband array was available, determining the location of the thermal fingerprint of the mantle plume in West Antarctica was impossible. While we are now guided by the new seismic mapping information, some ambiguities in location continue to exist. We attempt to examine this uncertainty by employing a single prototype plume placed at different locations.

##### 4.4.1. Plume A Statistics

The weak plume, Plume A, simulates a doubling of the geothermal heat flux directly above the mantle plume compared to the no plume experiment. The 540 locations selected in section 3.1.4 are regularly spaced every 50 km in both horizontal directions, and the simulations are performed independently. Figure 8 shows the local melt rate predicted above the mantle plume and is denoted by the differing color of the individual squares. Half of the locations experience basal melting in the presence of the mantle plume, with the highest  $\dot{m}_b^{(0)}$  reaching 64 mm/yr above the plume found under Thwaites Glacier. The median melt rate is  $\dot{m}_b^{(0)} \sim 13$  mm/yr. The total amount of basal meltwater production estimated under the model domain varies between 3.27 and 3.84 Gt/yr, depending on the location of the mantle plume. The Amundsen Sea Basin has basal friction and viscous dissipation supplying a strong contribution to melting. Excluding this basin, the total area-wide rate is reduced between 1.84 and 2.46 Gt/yr.

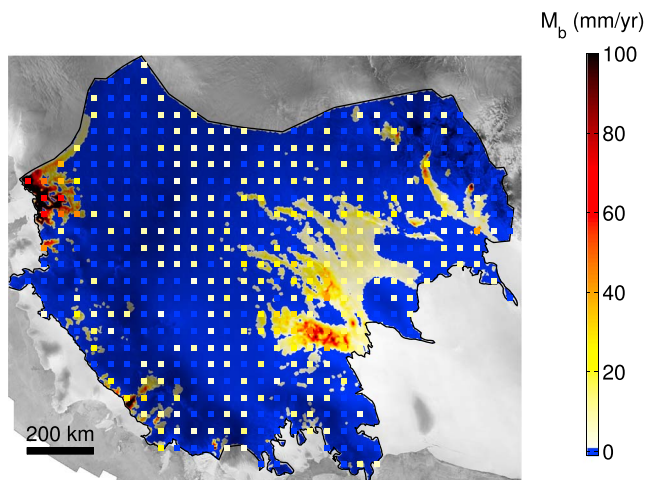


**Figure 9.** Same as Figure 8 with Plume B.

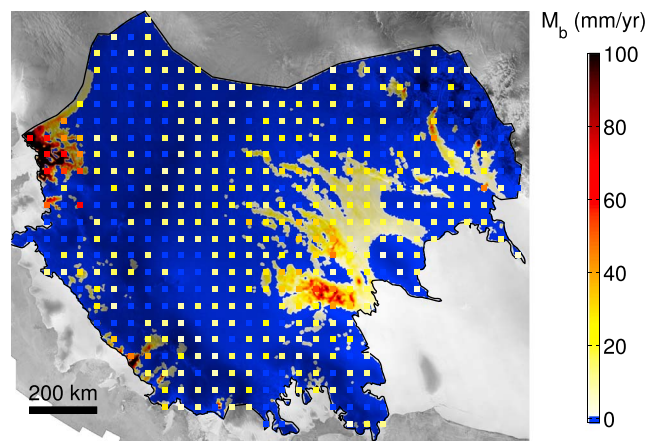


**Figure 10.** Same as Figure 8 with Plume C.

#### 4.4.2. Plume B Statistics

Plume B is similar in vertical thermal heat transfer to that of the Raton hotspot of northern New Mexico [e.g., Blackwell *et al.*, 2011; Zhao, 2015] with peak geothermal heat flux  $q_{\text{GHF}}^{(0)} = 180 \text{ mW/m}^2$  and radius,  $c$ , of 100 km (see Table 1 for plume characteristics).

Figure 9 shows the predicted melting rates on top of the plumes,  $\dot{m}_b^{(0)}$ . Two thirds of the locations experience basal melting in the presence of Plume B, including most areas in the ice streams feeding Ross Ice Shelf and the lower part of Thwaites Glacier. The highest values are found under Thwaites Glacier, with  $\dot{m}_b^{(0)} \geq 100 \text{ mm/yr}$ , while most areas are predicted to have  $\dot{m}_b^{(0)} \leq 40 \text{ mm/yr}$ . The distribution of melting rates is centered on  $\dot{m}_b^{(0)} \sim 19 \text{ mm/yr}$ . Over the entire basin, the predicted rate of total basal meltwater production varies between 3.28 and 4.05 Gt/yr. If we exclude the Amundsen Sea Basin, this range is reduced between 1.85 and 2.65 Gt/yr.

#### 4.4.3. Plume C Statistics

Plume C brings heat to the bottom of the crust, with  $D$  equal to 0 (see Table 1). The geothermal flux supplied to the base of the ice corresponds to a central value of  $258 \text{ mW/m}^2$ , somewhat similar to the value measured by Fisher *et al.* [2015]. Figure 10 shows the impact of Plume C on the predicted  $\dot{m}_b^{(0)}$  for the 540 simulations. In this case, 80% of the experiments simulate basal melting on top of the plume, with most melting rates below 45 mm/yr and the distribution centered on 23 mm/yr. The total basal meltwater produced over the model domain varies between 3.32 and 4.14 Gt/yr or 1.91 and 2.73 Gt/yr if we exclude the Amundsen Sea Sector.

#### 4.5. Impact of the Plume at Intraplate Scale

Table 2 summarizes the main characteristics of the basal conditions and amount of water produced for the different basins of the domain, for plumes of different intensities located in FR, ECR, and SLW. The three plume intensities reported (Plumes A, B, and C) create a maximum geothermal flux  $q_{\text{GHF}}^{(0)} = 128, 180, \text{ and } 258 \text{ mW/m}^2$ , respectively.

The Amundsen Sea Sector is not sensitive to variations in plume location and intensity, as frictional heat is high in this region. The total meltwater and mean basal melt rate only vary by a few percent (see Table 2). In stark contrast, hotspots placed in coastal positions, or anywhere within the Ross basin, have a significant impact on the rate of melt generation. This is consistent with the plume locations, as the FR plume is located in the Coastal Basin, while plumes of ECR and SLW are located in the Ross Basin and these regions do not have the natural tendency to create high frictional heat at the ice sheet base. The mean melt rate varies between 2.29 and 2.88 mm/yr for Ross basin and between 0.21 and 0.46 mm/yr for the Coastal region. Most of the predicted changes are within 200 km of the plume center. Both plume location and characteristics have a large impact on the amount and location of meltwater produced.

## 5. Discussion

Knowledge of subglacial conditions may lend important prognostic information about geothermal heat flux under the ice sheets [e.g., Siegert and Dowdeswell, 1996; Llubes *et al.*, 2006; Pattyn, 2010] and possible mantle

**Table 2.** Basal Melt Parameters at Basin Scale

Experiments	Entire Domain		Ross Basin		Coastal Basin		Amundsen Basin	
	Total Melt (Gt/yr)	Plume Melt (mm/yr)	Total Melt (Gt/yr)	Mean Melt (mm/yr)	Total Melt (Gt/yr)	Mean Melt (mm/yr)	Total Melt (Gt/yr)	Mean melt (mm/yr)
Plume A FR	3.18	10.5	1.44	2.29	0.34	2.39	1.41	6.33
Plume B FR	3.29	17.1	1.46	2.32	0.41	2.83	1.41	6.34
Plume C FR	3.34	26.0	1.46	2.33	0.46	3.17	1.41	6.35
Plume A ECR	3.22	0	1.57	2.50	0.27	1.85	1.38	6.45
Plume B ECR	3.37	6.2	1.64	2.62	0.28	1.90	1.38	6.50
Plume C ECR	3.46	20.8	1.75	2.78	0.28	1.90	1.38	6.50
Plume A SLW	3.27	7.1	1.63	2.59	0.21	1.43	1.43	6.19
Plume B SLW	3.34	14.9	1.75	2.78	0.21	1.44	1.45	6.19
Plume C SLW	3.40	24.4	1.81	2.88	0.21	1.44	1.45	6.19

origins [e.g., Rogozhina *et al.*, 2016]. The study of the subglacial environment is being improved with advances in both numerical ice flow modeling [Pattyn *et al.*, 2016] and observations [Young *et al.*, 2016]. The basal melting rate computed for the initialization experiment (see Table 1) based on the Shapiro and Ritzwoller [2004] geothermal flux reaches 5.77 Gt/yr for the entire model domain, which represents 4.67 mm/yr on average. This number agrees with the 5.3 mm/yr (65 Gt/yr for the entire AIS) computed by Pattyn [2010] using a geothermal flux adapted from Shapiro and Ritzwoller [2004] and Pollard *et al.* [2005].

### 5.1. Contrasting Regions

High geothermal flux values can be simulated with the mantle plume parameterization by adjustment of the Nusselt number and geometry of the plume, especially the depth to which the top approaches the base of the crust. ICESat-1 repeat tracks [Fricker and Scambos, 2009; Carter *et al.*, 2009; B. E. Smith *et al.*, 2009] map numerous active lakes that experience drainage events with volume change over 1 Gt on annual time scales in the Mercer and Whillans Ice Streams area. These events suggest the presence of a significant amount of basal water produced over these hydrologic basins [B. E. Smith *et al.*, 2009; Carter *et al.*, 2011].

Without a plume-like heating source, our simulations show that intrinsic heating and crustal sources do not provide enough energy to generate significant amounts of basal meltwater (Figures 4b and 11a) suggested by altimetry observations for the Mercer and Whillans Ice Streams, unlike what is observed for MacAyeal Ice Stream (Figure 4b). The presence of a mantle-derived heating similar to Plume B, which is capable of generating a maximum geothermal heat flux of 180 mW/m<sup>2</sup>, locally brings enough thermal energy to the ice base to be consistent with the inferred lake activity in the Mercer and Whillans ice area (Figure 11b). These observations suggest a local geothermal flux of at least 150 mW/m<sup>2</sup> is needed to properly simulate the observed subglacial lake activity observed. Plume C experiment leads to an additional meltwater production of 6% over the Ross Basin (Table 2), concentrated around the mantle heat source location. Furthermore, the headwaters of the basal flow are to be found at least 50 km upstream of SLW and stretch over large areas [Fricker and Scambos, 2009; B. E. Smith *et al.*, 2009]. Observations of ice shelf basal channels at the Antarctic periphery suggest that the Ross Ice Shelf receives an anomalously large percentage of the total basal meltwater transport from the ice sheet interior [Alley *et al.*, 2016]. The 3-D thermomechanical model employed here is in agreement with these observations, as only this part of our model domain, aside from the Thwaites glacier system, predicts large meltwater discharge. This suggests the presence of elevated geothermal heat flux in the uppermost parts of the Mercer and Whillans Ice Streams and over a region larger than simulated in our limited set of plume experiments. Low seismic wave velocity anomaly beneath SLW weakens with depth below 150 km [Heeszel *et al.*, 2016; Hansen *et al.*, 2014], suggesting a lithospheric rift origin for the enhanced heat flux. Geometrically complex rift features may produce elevated geothermal flux in the vicinity of the Whillans and Mercer Ice Streams.

In MBL remote sensing observations have not detected significant presence of active lakes, unlike what has been observed for many regions of Antarctica. This coastal area is covered with more limited sampling by ICESat-1 orbital tracks. However, even when accounting for this limited number of tracks, the area density of lakes is lower in MBL area than most other places in Antarctica. More advanced methods used recently

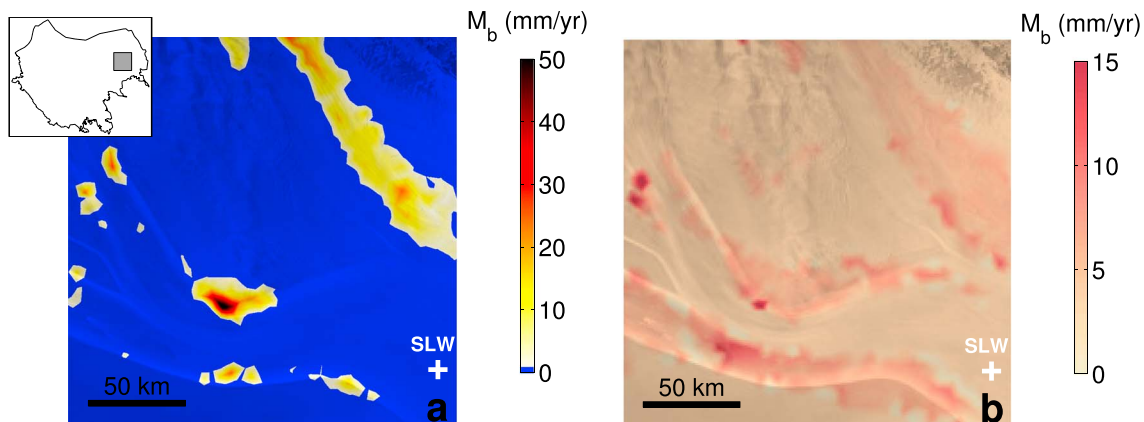


**Figure 11.** (a) Close-up view of basal melting (mm/yr) on the SLW area for the no-plume case and (b) difference between the basal melting (mm/yr) generated by Plume B located in SLW and the no-plume case. Notice the different color bars on both panels.

to determine elevation changes as the difference between surfaces also do not detect any alteration of the low lake density estimated for the MBL area [Babonis *et al.*, 2016]. It is therefore expected that basal melting is, in fact, quite limited in this region. From a theoretical standpoint, this is somewhat logical, as ice here has relatively slow velocity ( $\leq 300$  m/yr) and the ice thickness is less than 2000 m, and both are factors that inhibit local ice temperatures to approach the melting point [Pattyn, 2010].

The mantle and ice flow models simulated in this study suggest that a weaker plume is viable in MBL. Geophysical and geochemical data support the hypothesis of a moderate and fairly young mantle plume that advects heat into MBL, likely located under the ECR [Sieminski *et al.*, 2003; LeMasurier, 2008; Lloyd *et al.*, 2015]. If the peak heat transport at present day is near  $180$  mW/m $^2$ , similar to the Plume B experiment, our numerical experiments predict significant amounts of water to be present (Figure 5b and Table 2), clearly conflicting with observation. Plumes producing a geothermal flux lower than  $150$  mW/m $^2$  predict a relatively small amount of basal meltwater in this area, compatible with observations of subglacial conditions (Figures 5d and 6d). Such values are higher than observed at the Cape Verde hotspot, where measured geothermal heat flux most likely does not exceed about  $75$  mW/m $^2$  [Courtney and White, 1986]. Higher plume-related geothermal flux, as high as those measured by Fisher *et al.* [2015], is unlikely for this region, as they generate basal water at rates of a couple centimeters per year, inconsistent with observations. The rates of Antarctic Plate translation and rotation with respect to the mantle frame are limited over the past 75–85 Ma [Lawver *et al.*, 1991; Gripp and Gordon, 2002; Becker *et al.*, 2015]. It might be speculated that a relatively broad-scale plume impinged upon the continent during Late Cretaceous plate breakup, having a less concentrated impact on the lithosphere than we have modeled in our series of analogues to the Yellowstone plume. The heat supply associated with renewed volcanism initiated at about 30–20 Ma could be interpreted as deriving from a less vigorous mantle upwelling.

## 5.2. Caveats

A limitation of our simulations comes from the thermal steady state assumption made to derive the thermal state of the ice sheet. This assumption has minor impact on century-scale simulations of the Greenland ice sheet evolution [Seroussi *et al.*, 2013]. However, variations in surface temperature and ice sheet velocities influence both the ice thermal state and ice sheet basal conditions. The goal of the present study is to assess the range of basal conditions under the WAIS and to provide new bounds on the geothermal heat flux in light of newly emerging seismic mapping of the mantle. Quantitative mapping of basal melting rates is, therefore, beyond the scope of our study. Water gained and lost by hydrodynamic melting and freezing is unaccounted for here. However, the low hydraulic gradients in Antarctica likely limit this water amount to less than 1% of the water budget [Carter *et al.*, 2009].

The mantle plume parameterization has limitations, as it does not capture details of mantle plume growth or head evolution. However, it produces realistic geothermal heat flux at the base of the Antarctic ice sheet, heat flow, and buoyancy flux within the range estimated and allows sampling a variety of plume characteristics.

### 5.3. Future Challenges

What little we yet know about subglacial hydrology comes exclusively from altimetry mapping, radar return signals, velocity accelerations, and some limited seismic and borehole information [e.g., *Carsey et al.*, 2002; *Winberry et al.*, 2009; *Siegfried et al.*, 2016]. Assembling these data to form a subglacial water budget may provide us with a crude approximation of the water production rates. *Carter et al.* [2011] estimate that subglacial water is interconnected to the entire hydrologic basin and that these lakes temporarily store most of the subglacial water that passes through them. Radar sounding measurements hold some promise to provide first-order observations of basal water [*Schroeder et al.*, 2013; *Young et al.*, 2016] and attenuation rate through the ice column [*Schroeder et al.*, 2016], from which temperatures within the ice might be derived. This would allow more sophisticated basal heat flux models to be explored. Satellite altimetry acquired over the past decade has proven to be essential to detect the presence and activity of subglacial lakes [*Fricker et al.*, 2007; *Carter et al.*, 2011; *Fricker et al.*, 2016; *Kim et al.*, 2016] and is a key observation that allows us to come to the conclusion that a very high basal heat flux can be ruled out in MBL.

Determining the magnitude and spatial distribution of basal melting is a central issue for modeling ice sheet evolution. Internal water transport and volumetric generation rate are fundamental to the problem of predicting future susceptibility to rapid retreat [e.g., *Bell*, 2008; *Creyts and Schoof*, 2009]. Water at the base of the Ross ice streams may be a prime cause of the efficient evacuation of ice during the Last Glacial Maximum, in spite of the great advancement of the grounding line over the Ross Embayment during lowering of sea level [e.g., *Bromley et al.*, 2012; *Ivins et al.*, 2013]. Modeling the complexities of the last phase of deglaciation of the eastern Ross Shelf between 2.5 and 1.5 ka [*Yokoyama et al.*, 2016] should consider how basal water lubrication altered upstream dynamics under the continent bound ice sheet.

## 6. Conclusions

We have investigated here the basal conditions of West Antarctica using a 3-D full-Stokes thermomechanical ice flow model and geothermal heat flux generated by a mantle plume parameterization. Recent seismic imaging supports the idea that a mantle plume has ascended from below the 660 km seismic discontinuity beneath the West Antarctic crust, possibly in two or more phases. During the past decade, mapping from space has clearly identified events that can only be interpreted as pulsations of water transport at the base of WAIS [e.g., *Fricker et al.*, 2007; *Siegfried et al.*, 2014; *Kim et al.*, 2016]. A ubiquitous and somewhat sustained water transport is observed under the Ross ice streams [*Siegfried et al.*, 2016]. We show that intrinsic heating beneath the Whillans and Mercer Ice Streams is quite limited and that geothermal heat flux above 150 mW/m<sup>2</sup> over a large region plays an important role in water production. The heating likely has mantle provenance, potentially caused by a rift in the lithosphere.

A plume source for the MBL dome is certainly possible, but it should not elevate surface heat flux to values exceeding 150 mW/m<sup>2</sup>, as this would generate excessive basal water. This explanation of limited plume heat transport, therefore, provides the most logical resolution of the apparent paradox of limited lake density in MBL and the combined seismic and petrological data supporting the presence of a plume.

## Appendix A: Buoyancy Flux and Vertical Heat Transport Within the Plume

While some debate continues over both theory and observation of mantle plumes, the relevant laboratory and numerical fluid dynamic experiments began to be assembled in the early 1980s [e.g., *Olson et al.*, 1993]. In the decades that followed, the basic concepts of plume heat and mass transport across the mantle began to fully emerge, providing essential scaling principles that aid in quantifying plume related heat transport to the base of the ice sheets.

We assess here the time that is reasonable to assume for the growth of a finite-amplitude plume into the environment of West Antarctica on time scales short ( $\sim$ 20 Ma) compared to the time of late Gondwana breakup (at about  $107 \pm 5$  Ma, [*Storey et al.*, 1999]). Older plumes and their heads are more greatly influenced by lateral mantle advection and will tend to be more spread out than will younger ones of relatively tight spatial confinement.

The amplitude of thermal convection is connected to the dimensionless parameter known as the Rayleigh number,  $Ra$ . In classical free convection, wherein a layer is heated from below, this is the ratio of gravitational

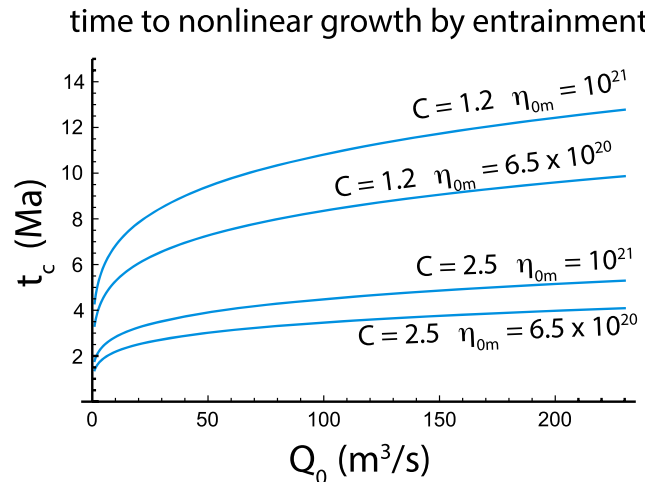


**Figure A1.** Time to nonlinear growth ( $t_c$ ) as a function of starting volume flux ( $Q_0$ ) using equation (A3). The values of  $\alpha_m$ ,  $\Delta T_s$ , and  $\rho_m$  are  $2.10^{-5} \text{ }^\circ\text{C}^{-1}$ ,  $250 \text{ }^\circ\text{C}$ , and  $3950 \text{ kg m}^{-3}$ , respectively. Note the strong dependence on  $C$ , an experimentally based parameter with  $0.5 \leq C \leq 4.0$ , according to Van Keeken [1997].

potential energy released by buoyant motions to the energy lost in viscous dissipation in that same motion (less conductive loss) [e.g., Malkus, 1954]. In contrast, although plumes involve buoyant driven vertical heat transport, they must be described in terms of transient fluid motions. Many fluid dynamic complexities are beyond the scope of this paper, and hence, we limit the discussion to the most essential transport characteristics of the mantle plume theory. These include the time scale,  $t_c$ , of the emerging plume, or the time required for evolution to a state where entrainment of surrounding mantle material during rise dominates the volume increase. After this time, the volume of entrained material grows nonlinearly, as does the speed of rise. A thermal instability occurs with some initial lateral temperature difference  $\Delta T_s$ , and depth,  $d$ .

Griffiths [1986] defined the Rayleigh number for plumes as follows:

$$Ra_p \equiv B/\kappa_m \eta_{0m}, \quad (\text{A1})$$

where  $\kappa_m$  and  $\eta_{0m}$  are mantle thermal diffusivity and effective viscosity, respectively.  $B$  is a measure of the plume material buoyancy and is time dependent as it rises:

$$B = g \rho_m \alpha_m \Delta T_s \cdot Q(t - t_0), \quad (\text{A2})$$

where  $\rho_m$ ,  $\alpha_m$ , and  $Q(t)$  are, respectively, the mantle density, coefficient of thermal expansion, and the source volume flux (in  $\text{m}^3/\text{s}$ ) that is generally a function of time,  $t$ . This latter flux is initially a linear function of time, but as mantle material becomes entrained in the upwelling thermal, it grows as  $t^p$ , with  $5/4 \leq p \leq 9/4$  [Van Keeken, 1997]. Griffiths and Campbell [1990] also defined the plume heat flow (in  $\text{J/s}$  or watts) as  $Q_{\text{plume}} = \rho_m c_p Q(t) \Delta T_s$ , with  $c_p$  the specific heat.

A series of numerical and laboratory experiments by Van Keeken [1997] and Weinberg [1997] clarified the typical evolution in the presence of realistic rheological laws for mantle rock, better defining the nonlinear growth phase after reaching critical time:

$$t_c - t_0 = \left( \frac{C^{-2} \eta_{0m}}{g \rho_m \alpha_m \Delta T_s} \right)^{3/5} \cdot Q_0^{1/5}, \quad (\text{A3})$$

where  $Q_0$  is the volume flux at  $t = t_0$  and  $C$  is an empirical nondimensional parameter (see Figure A1). Weinberg [1997] used the average volume flux prior to  $t_c$  ( $Q_0$ ) to estimate rise times, plume temperatures, and head radii as they approached the top of the upper mantle. Experiments by Van Keeken [1997] showed that a typical rise velocity across the entire mantle is roughly  $3.5 \text{ cm/yr}$ . Cserepes and Yuen [2000] reasonably hypothesized plume volume formation at midmantle depths, below the mantle transition zone at  $660 \text{ km}$  depth. Such plumes are predicted to arrive to the base of the crust in just  $20 \text{ Ma}$ . Using the suggested ranges and parameters noted in the appendix of Weinberg [1997], we calculate  $t_c$  in Figure A1.

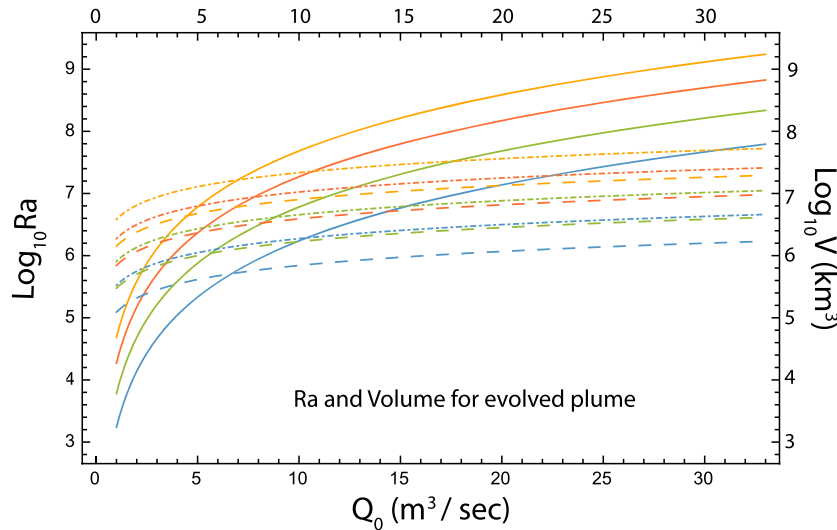


**Figure A2.** Effective  $Ra_p$  (solid lines) and mature plume head volume  $V$  (dash-dotted and long dashed lines for 28 Ma and 18 Ma, respectively) as a function of starting flux,  $Q_0$ , using equation (A3). Scaling is  $Ra_p = g\alpha_m \Delta T_s Q_0^3 / \eta_{0m} \kappa_m^4$  and  $V = (4C/9)^{3/2} \kappa^{15/4} Q_0^{-3/2} Ra_p^{3/4} t^{9/4}$  [Griffiths, 1986]. Values of  $\alpha_m$  and  $\Delta T_s$  are similar to Figure A1. Values used for  $C$  and  $\kappa_m$  are 2.8 and  $2 \times 10^{-6}$  m<sup>2</sup>/s, respectively. Orange, red, green, and blue colors correspond to  $\eta_{0m} = 2.5, 6.5, 20$ , and  $65 \times 10^{20}$  Pa s, respectively.

### A1. Thermal Energy Transport

As plumes rise throughout the volume of the mantle, they naturally cool by diffusion of their heat to the cooler surroundings and by entrainment of adjacent mantle into the rising plume head. Using the scaling principles for mature plumes of Griffiths [1986] and Griffiths and Campbell [1990], it is possible to derive asymptotic solutions with  $t \gg t_c$  for the temperature anomaly. As the plume rises from an initial rest state at an unstable mantle boundary, it grows to a height,  $z_{rise}$ . Asymptotic solutions above predict the cooling of the anomaly in time in proportion to  $1/z_{rise}$ , as well as the rise in volume,  $V$ , and net buoyancy,  $B$ . Rearranging equation (17) from Griffiths and Campbell [1990] allows the anomaly being predicted in terms of  $Ra_p$  and  $\eta_{0m}$ .

The temperature anomaly with height of rise in the mantle from starting position  $z_{rise} = 0$  is predicted to be

$$\Delta T = \xi(C) \Delta T_s^{\frac{2}{3}} \left[ \frac{\kappa_m \eta_{0m} R a_p}{\alpha_m g} \right]^{\frac{1}{3}} \cdot \frac{1}{z_{rise}}, \quad (\text{A4})$$

with  $\xi(C) \equiv (27/80)(6/\pi)^{2/3} C^{-2}$ . Griffiths and Campbell [1990] also generated scaling principles for the mature plume head volume,  $V$ , and effective  $Ra_p$ . We show values appropriate for a plume with a size corresponding to the Yellowstone or Crozet hotspots [e.g., Campbell and Griffiths, 1990; R. B. Smith et al., 2009] in Figure A2. Note that the  $Ra_p$  (solid lines in Figure A2) values are orders of magnitude above the critical value for thermal instability ( $Ra_c \sim 700-1400$  for fluids heated from below, regardless of stress boundary conditions).

For these supercritical values, heat transport by vertical convective motion is highly efficient. In a thermally convecting fluid transport system the time averaged heat flux,  $q_H$ , traversing the entire system toward the cooler surface is as follows:

$$q_H = -k \frac{\partial \bar{T}}{\partial z} + \rho C_V \bar{\omega} \bar{T}, \quad (\text{A5})$$

where  $T$  is the total convecting plus conductive temperature,  $\omega$ , the vertical component of velocity,  $\rho$ , the density,  $C_V$ , the heat capacity at constant volume,  $k$ , the fluid conductivity and (...) represents time-average [Malkus, 1954]. The efficiency of convective heat transport is also measured by the ratio:

$$Nu \equiv \frac{q_H}{\rho C_V \beta_0}, \quad (\text{A6})$$

where  $\beta_0$  is the vertical temperature gradient in the absence of convection. This ratio is also called the Nusselt number. Using the scaling for free convection with no internal heat sources, we estimate that

$$Nu = 0.77 \left( \frac{Ra}{Ra_c} \right)^{\frac{1}{3}} \quad (A7)$$

following [Turner, 1973]. This efficiency measure exceeds 300 for all values of mantle viscosity computed in Figure A2 for source values  $Q_0 \geq 10 \text{ m}^3 \text{ s}^{-1}$ .

## A2. Plume Approximation for Heat Transport

The temperature anomaly advected to the near lithospheric environment is also efficient. Assuming  $Ra_p \simeq 2 \times 10^5$ ,  $\eta_{0m} \simeq 0.65 \times 10^{21} \text{ Pa s}$ ,  $\kappa_m \simeq 1.2 \times 10^{-6} \text{ m}^2/\text{s}$  (see Gibert et al. [2003] for upper mantle estimates),  $\Delta T_s \simeq 300^\circ\text{C}$  and all other values similar to Figure A2, we estimate that the anomaly is reduced to  $\Delta T_s \simeq 240^\circ\text{C}$  while rising 1000 km. However, numerical experiments by Weinberg [1997] revealed that this simple scaling relation breaks down for general prediction of temperature anomalies arriving to the lithospheric environment. Furthermore, Van Keken [1997] demonstrated the limits of the asymptotic solutions. He performed experiments consistent with the exponent for time dependence of entrainment enhanced volume increase limited to  $p < 5/4$ ; supercritical growth was difficult to reach in many of his numerical experiments. Similar results were found by Weinberg [1997], along with numerical predictions of the rise rate, and ultimate value for  $\Delta T$ , substantially diverging from the simple relation of equation (A7).

What then are the scaling properties to be employed to describe a simple model of heat transport to the lithospheric environment? Several compelling facts can be assembled from the collection of laboratory and numerical experiments. All of the basic parameters that define the Rayleigh number and buoyancy in equations (A1) and (A9) are appropriate, and entrainment is part of the thermomechanics of the ascent of the mantle plume. It is also safe to assume conservation of the thermal energy on rise:

$$d(\Delta TV)/dt = Q_0 \Delta T_s \quad (A8)$$

ignoring latent heat and viscous dissipation, which are reasonable assumptions for buoyant material rise in the mantle [e.g., Busse, 1979].

In Appendix B these parameters, along with the deep heat flow rate,  $Q_{\text{plume}}$ , will be employed for developing systematic and analytic relations for the heat flow arriving just below the mechanical lithosphere of West Antarctica. The geometry of the approximation is shown in Figure C1. The depth to the top of the plume from the base of the crust of the Earth is  $D$ , and the depth to the midpoint of the unstable, but mature, plume is  $D + \mathbf{z}_\epsilon$ . At the base of the unstable layer, an anomalous temperature contrast  $\Delta T_s$ , or “starting plume” temperature is to be assumed. The time scale over which this transition to a fully developed plume occurs has been the focus of a number of studies in the 1990s. The plume head forms by a circulatory flow, before the rising material experiences any stress or flow interaction with the surface or lithosphere [Daly and Raefsky, 1985; Griffiths and Campbell, 1990].

The buoyancy flux,  $B_{\text{plume}}$ , transported by the mantle plume with the default parameters (see Table C1) can be computed based on the mantle plume parameterization. Methods for a full numerical plume treatment are described by Yoshida [2012] using the vertical velocity within the plume structure. As our parameterization has only a proxy for vertical advection of heat and therefore no explicit vertical velocity, we approximate  $Q_{\text{plume}}$  as follows:

$$Q_{\text{plume}}(z) = \rho_m C_V \int_S q_{\text{plume}}(z) dS, \quad (A9)$$

where  $\rho_m$  is the mantle/lithosphere density just above the plume and  $S$  a cross-sectional area that lays in a plane orthogonal to the model plume vertical axis, at a distance  $\delta$  just above the top of the plume. Here we write  $q_{\text{plume}}$  just as a simple function of  $z$ , but it is a highly complicated algebraic expression developed in the Mathematica coding language, dependent upon all three spatial coordinates,  $x, y, z$ . Further discussion of this functional form and dependency on  $\epsilon$ , radius  $c$ , height  $\mathbf{z}_\epsilon$ , and distance above the top of the parameterized model plume, etc., is given below in Appendix B. The buoyancy flux then follows as:

$$B_{\text{plume}}(z) = \frac{\alpha_m}{C_V} Q_{\text{plume}}(z). \quad (A10)$$

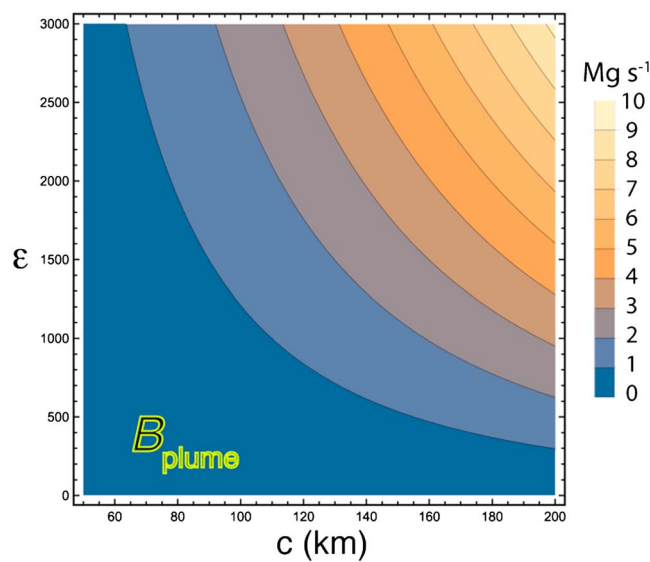


**Figure A3.** Buoyancy flux (in Mg/s) produced by the mantle plume parameterization and the buoyancy flux formula (equation (A10)) as a function of plume radius and  $\varepsilon$ . Evaluation of the integral is computed 10 km above the plume top.

Figure A3 shows that  $B_{\text{plume}}$  varies between 0.1 and 10 Mg/s depending on the plume radius and  $\varepsilon$ , in general agreement with estimations that vary between 0.25 Mg/s for Yellowstone [B. E. Smith et al., 2009] and 8.7 Mg/s for Hawaii [Sleep, 1990].

## Appendix B: Practical Consequences of the Plume Hypothesis

The primary interest of examining the mantle plume structure in greater detail in this paper is to examine the viability of the hypothesis itself and ask if the existence of the ice sheet in its present state is, in fact, viable when supplied with the basal heat flux enhancement that accompanies active late Cenozoic mantle plumes. Toward this end, we construct a detailed model that enables us to parameterize the general geometry and vertical heat transport enhancement of the mantle plume. This involves a structure that enables vertical heat transport by relatively rapid (by comparison to other solid mantle deformation) vertical mantle flow. One simplification is to allow the structure being approximated by an elongated, thin body of enhanced thermal conductivity. The enhancement factor should be related in some way to the nondimensional parameters that describe dynamic models of mantle plumes.

The mathematical formulation of the solution from the standpoint of classical potential theory is described by Landau et al. [1984] and involves elliptical integrals that follow from applying Green's theorem. The solutions are discussed by Carslaw and Jaeger [1986]. Our use of this theory will assume that the plume is vertically standing and is adequately represented by a prolate ellipsoid having material of high conductivity embedded in an infinite medium of lower conductivity,  $k_m$ , which we take as the mean conductivity of mantle rock (Figure C1). The interior of the prolate ellipsoid has a higher conductivity and the ratio of “inside” to “outside” conductivities will be given as  $\varepsilon$ . As discussed for plume thermodynamical scaling laws,  $Ra_p$  greatly exceeds critical value for growth of thermal instability, and therefore, we assert that a good approximation is  $\varepsilon \approx Nu$ . Rocks inside the modeled mantle plume have an artificially high model thermal conductivity, as this provides a convenient mathematical way to modulate the vertical heat transport associated with advection. This assumption is not a good model for examining any other thermally related properties of mantle lithosphere, yet it quite adequately represents the geometry and vertical transport with respect to the bottom of the ice sheet and its interior.

### B1. Analytic Plume Vertical Heat Transport

The solution of the thermal equation reduces to applying the integral form of Green's identity to Laplace's equation with Dirichlet conditions of the second type. With  $\mathbf{z}'/2$  and  $c$  the semi major and minor ellipsoid axes, the resultant integral equations involve the root,  $\lambda$ , of the following:

$$\frac{z'^2}{(\mathbf{z}'^2/4) + \lambda} + \frac{x'^2 + y'^2}{c^2 + \lambda} = 1, \quad (\text{B1})$$

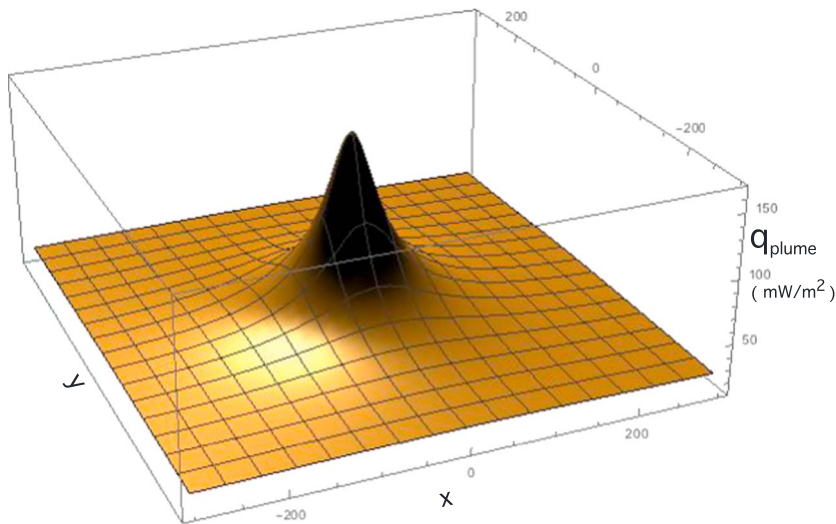


**Figure B1.** Example of heat flux in  $\text{mW}/\text{m}^2$  ( $q_{\text{plume}}$  at  $z_0 = 0$ , no crust heat included). Geophysical parameters for the mantle plume are  $k_m = 2.22 \text{ W}/(\text{m}\cdot\text{°C})$ ,  $\mathbf{z}_\ell = 525 \text{ km}$ ,  $\varepsilon = 300$ ,  $D = 15 \text{ km}$ ,  $c = 125 \text{ km}$ , and  $\partial T_{\text{bg}}/\partial z_0 = 11 \text{ °C}/\text{km}$ . The rationale for the assumed value for  $\varepsilon$  is given in section A1. Values of “ $x$ ” and “ $y$ ” are in kilometers.

with coordinates  $x', y', z'$  shifted to the center of the ellipsoid as in Figure C1. Our interest is to express the heat transport and solid Earth quantities, so with the origin  $(x_0, y_0, z_0)$  at, or near, the surface of the Earth and axis  $z_0$  oriented downward as shown on Figure C1. The analytical representation of the heat transport associated with the plume includes an essential geometrical factor:

$$\mathcal{A}_o \equiv \frac{1 - \bar{\epsilon}^2}{\bar{\epsilon}^3} \cdot \left[ \frac{1}{2} \log_e \left( \frac{1 + \bar{\epsilon}}{1 - \bar{\epsilon}} \right) - \bar{\epsilon} \right] \quad (\text{B2})$$

that results in applying the continuity conditions at the boundary between the idealized prolate ellipsoidal shape of the plume and the adjacent assumed homogeneous mantle. Here the ellipticity,  $\bar{\epsilon}$  of the prolate-shaped plume (Figure C1) is as follows:

$$\bar{\epsilon} \equiv \sqrt{\frac{\mathbf{z}_\ell^2 - 4c^2}{\mathbf{z}_\ell^2}}. \quad (\text{B3})$$

Symmetry considerations allow the solutions to the boundary value problem for Laplace’s equation for temperature and vertical conductive heat transport to be represented exterior to the mantle entraining rising plume. It is assumed that the surrounding mantle has a constant steady background vertical temperature gradient, applicable to  $|x'|, |y'| \gg \mathbf{z}_\ell$ . Toward this purpose, a solution of the diffusion equation for this region is constructed from the following:

$$\mathcal{A}(x', y', z') \equiv \frac{1 - \bar{\epsilon}^2}{\bar{\epsilon}^3} \cdot \left[ \frac{1}{2} \log_e \left( \frac{1 + \bar{\epsilon}^*}{1 - \bar{\epsilon}^*} \right) - \bar{\epsilon}^* \right] \quad (\text{B4})$$

$$\bar{\epsilon}^*(x', y', z') \equiv \sqrt{\frac{\mathbf{z}_\ell^2 - 4c^2}{\mathbf{z}_\ell^2 + \lambda}}. \quad (\text{B5})$$

For example, the spatial dependence on the plane  $z' = -(D + \mathbf{z}_\ell)$  (or equivalently,  $z_0 = 0$ ) is accounted for by  $\mathcal{A}$ :

$$\lambda_s(x', y') = \frac{1}{4} \left\{ \sqrt{\mathbf{z}_\ell^2 (x'^2 + y'^2) + 4c^2 [\mathbf{z}_\ell D + D^2] + p_s^2(x', y')} + p_s(x', y') \right\}, \quad (\text{B6})$$

with  $p_s(x', y') \equiv \mathbf{z}_\ell D - c^2 + D^2 + x'^2 + y'^2$  and where we use the subscript  $s$  to indicate evaluation near the Earth’s surface.

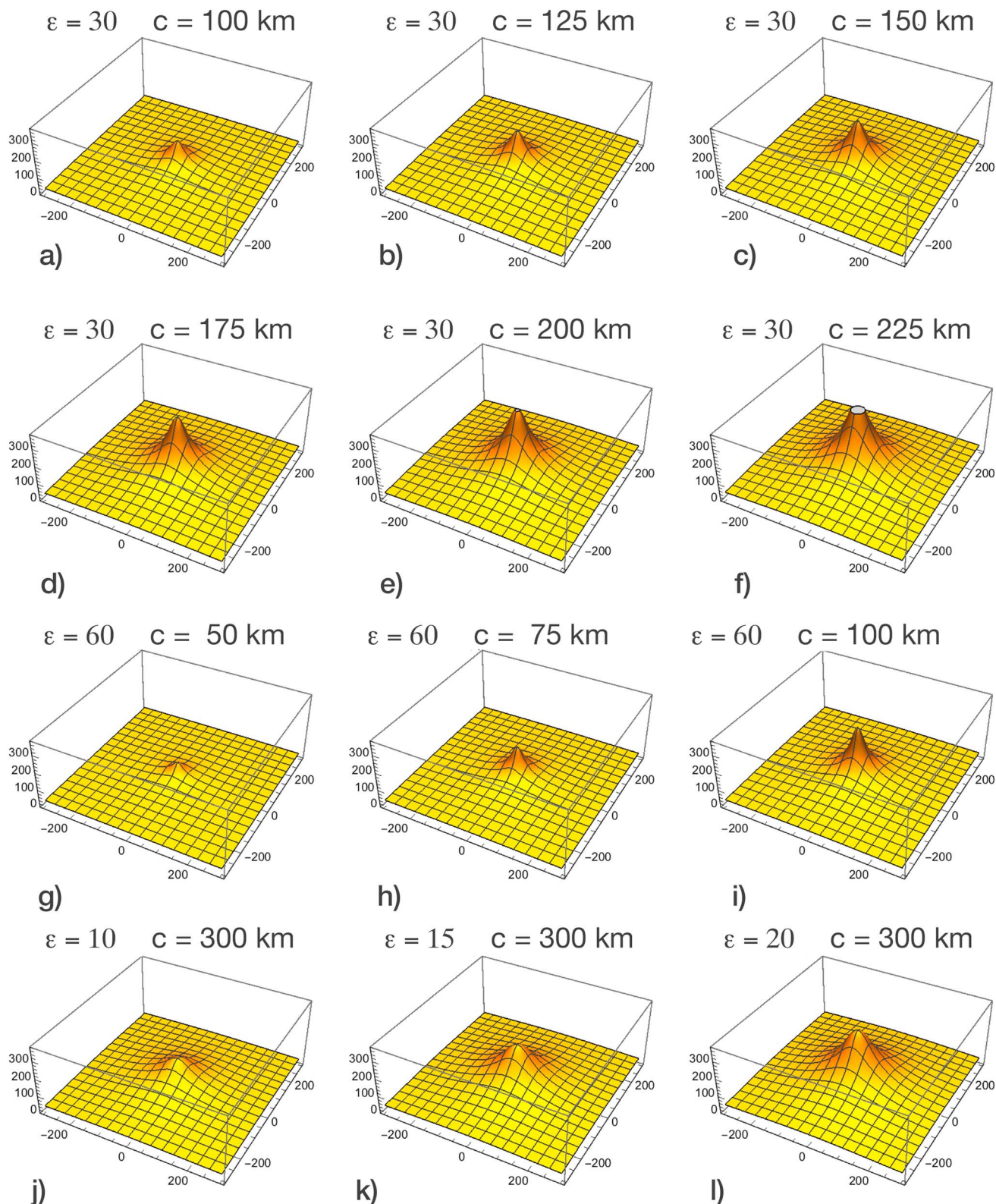


**Figure B2.** Plume model heat flux at  $z_0 = 0$ , as in Figure B1, but with variations in Nusselt number ( $\varepsilon$ ) and radius ( $c$ ). The top of the plume is located at a depth  $D = 20$  km below the crust (see Figure C1). (a–f) Increase with  $c$  at constant  $\varepsilon$ . (g–i) Similar increases in  $c$  but at twice the value of  $\varepsilon$ . (j–l) The effect of increase in  $\varepsilon$  at constant  $c = 300$  km. This display reveals the nonunique relation between plume parameterization and surface heat flux.

## B2. Steady Heat Transport to the Base of the Crust

The background heat transport away from the plume is as follows:

$$q_{\text{bg}}(x_0, y_0, z_0) = -k_m \hat{k} \cdot \nabla T_{\text{bg}}, \quad (\text{B7})$$

where we use the subscript bg for properties away for the plume. The 3-D expression for  $\lambda$ , an expression for the plume-enhanced vertical heat transport outside the perimeter of the plume, here idealized by the boundary of the prolate spheroid, follows as

$$q_{\text{plume}}(x_0, y_0, z_0) = -k_m \frac{\partial T_{\text{bg}}}{\partial z_0} \left\{ 1 + \Upsilon(\epsilon - 1) \cdot [\mathcal{A} + (z_0 - D - \frac{z_\ell}{2}) \frac{\partial \mathcal{A}}{\partial z_0}] \right\} \quad (\text{B8})$$

where

$$\Upsilon(\epsilon, z_\ell, c) \equiv [1 + (\epsilon - 1)\mathcal{A}_o]^{-1}.$$

The model prediction of heat flux at the Earth's Moho (crust-mantle interface) is found by setting  $z_0 = 0$ . In the case when there is negligible heat production within the crust, this near-surface value for  $q_{\text{plume}}(x_0, y_0, 0)$  will closely match the prediction of heat flux,  $q_{\text{GHF}}$ , into the base of the ice sheet. The two-dimensional (2-D) spatial dependence of a typical solution using equation (B8) is shown in Figures B1 and B2. The relationships that are formed for the analytical model are highly nonlinear in their coupling of all spatial and geometrical parameters. This manifests a nonuniqueness in relating  $q_{\text{plume}}$  to all the geometrical and the Nusselt number. This fact is well depicted in Figure B2 (also see supporting information), wherein we explore the  $q_{\text{plume}}$  dependency on  $c$  and  $\epsilon$ . Further dependency on  $D$  is discussed in the supporting information and may be found to be especially relevant to oceanic hotspots.

More than one plume may be accounted for by replacing the first term in brackets on the right-hand side of equation (B8) from "1" to "1/N," where "N" is the number of plumes at different locations but of identical geometry and transport properties. We caution that the surface flux has asymmetrical patterns. A view from recent seismic tomography of Yellowstone plume crust mantle reveals asymmetries that might also characterize the hotspot in MBL [Huang *et al.*, 2015].

## Appendix C: Crustal Heat Generation

In this appendix, we describe how the crustal model transfers heat from the lithosphere across the crust to the base of the ice sheet. It is important to include the radiogenic heat sources of the crust. The cratonic crust of East Antarctica is generally of either Archean or Proterozoic age [Fitzsimons, 2003; Heeszel *et al.*, 2013]. Hence, models from other continental provinces of similar age may be employed for constructing the radiogenic sources that supply heat to the surface of bedrock. Post Middle Cretaceous West Antarctic tectonic history, in contrast, is complicated by subduction, back-arc tectonics, and rifting [Weaver *et al.*, 1994; Dalziel and Lawver, 2001; Eagles *et al.*, 2004; Torsvik *et al.*, 2008]. Consequently, the evolution of the modern crust likely involves recycling of mantle, crustal, and lithospheric elements. The tectonic involvement with mantle dynamics makes an assessment of the radiogenic content of the crust during late Cenozoic time more ambiguous than that of the large craton to the east.

With this background in mind, we model the plume heat transport to the base of the ice sheet through a crustal model with two layers. The layers, of thickness  $H_i$  and temperature  $T_i$  are denoted "1" and "2" for upper and lower crust, respectively (see Figure C1). We use the symbols  $q_b$  and  $\tau_b$  as the heat flux and temperature at the base of the crusts. We solve the steady state diffusion equation for the two layers with boundary conditions,  $T_1(0) = \tau_b$ ,  $T_1(H_1) = T_2(H_1)$ ,  $k_1 \partial T_1(H_1) / \partial z = k_2 \partial T_2(H_1) / \partial z$ ,  $\partial T_2(z_m) / \partial z = q_b / k_2$ , with  $z_m$  the total crust thickness.

Using the first derivative of the solution in the upper crust evaluated at  $z = 0$ , the heat flux to the surface may be easily computed as follows:

$$q_{\text{GHF}} = [A_1 H_1 + A_2 (z_m - H_1)] + q_b, \quad (\text{C1})$$

with  $A_i$  the crust heat production in layer  $i$ .

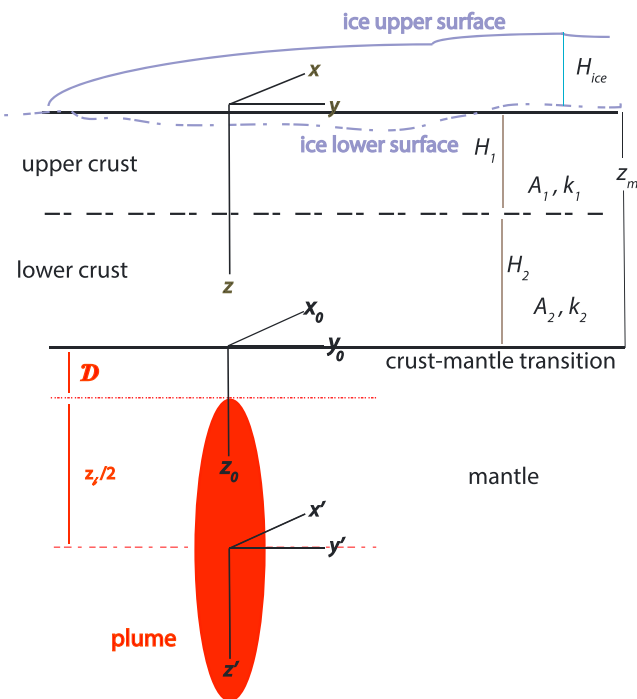


**Figure C1.** Schematic of the crust and mantle plume sources of heat transport to the base of the ice sheet. The primed frame is centered in the mantle plume, the “0” frame at the base of the crust, and the  $x, y, z$  frame at the surface of the solid silicate Earth.

**Table C1.** Model Parameters

Parameter	Value	Description
$z_m$	31.4 km	Crust thickness
$H_1$	14 km	Upper layer crust thickness
$A_1$	$1.33 \times 10^{-6} \text{ W/m}^3$	Upper crust heat production
$A_2$	$0.27 \times 10^{-6} \text{ W/m}^3$	Lower crust heat production
$D$	Variable	Mantle plume depth below the crust
$c$	Variable	Mantle plume radius
$\epsilon$	Variable	Ratio of the inside to outside conductivity
$z_p$	Variable	Mantle plume length
$\partial T_{\text{bg}} / \partial z_0$	$13^\circ \text{ C/km}$	Linearized gradient of the background temperature
$k_m$	$2.4 \text{ W/m}^\circ\text{C}$	Mantle conductivity
$Q_{\text{plume}}$	Variable (J/s)	Plume heat flow
$B_{\text{plume}}$	Variable (Mg/s)	Plume buoyancy flux
$q_{\text{plume}}$	Variable ( $\text{mW/m}^2$ )	Plume induced geothermal heat flux
$q_{\text{GHF}}$	Variable ( $\text{mW/m}^2$ )	Geothermal heat flux
$q_{\text{GHF}}^{(0)}$	Variable ( $\text{mW/m}^2$ )	Geothermal heat flux on top of the plume
$\rho_i$	$917 \text{ kg/m}^3$	Ice density
$k_i$	$2.4 \text{ W/m}^\circ\text{C}$	Ice thermal conductivity
$L_i$	$334 \text{ kJ/kg}$	Ice latent heat
$T_b$	Variable ( $^\circ\text{C}$ )	Basal ice temperature
$T_b^{(0)}$	Variable ( $^\circ\text{C}$ )	Basal ice temperature on top of the plume
$\dot{m}_b$	Variable (mm/yr)	Basal ice melt rate
$\dot{m}_b^{(0)}$	Variable (mm/yr)	Basal ice melt rate on top of the plume

A baseline study of heat generation and flux in cratonic terrain was performed by *Mareschal et al.* [2004], who determined that a radiogenically enriched layer of 10 km thickness overlays a crustal layer typical of Archean crust in northern Canada. Using values for  $A_1$  and  $A_2$  equal to  $1.7 \times 10^{-6}$  W/m<sup>3</sup> and  $0.4 \times 10^{-6}$  W/m<sup>3</sup> for the upper and lower layers, respectively, from this study, as well as  $H_1 = 17$  km and  $z_m = 38$  km, the calculated heat flux from the crustal radiogenic heating is 37.3 mW/m<sup>2</sup>. Important sources for generating a surface heat flux near the values of 97 mW/m<sup>2</sup>, as suggested by *Damiani et al.* [2014] for MBL, must be found in the mantle, for here we have actually used the enriched values for radiogenic heating in this calculation. Our model will nevertheless include a two-layer crust of thickness corresponding to that of the MBL. The properties used for our study are based on the average values determined by *Chaput et al.* [2014]:  $z_m = 31.4$  km, with an upper crustal thickness  $H_1 = 14$  km. These are typical of moderately extended continental terrain [e.g., *Campillo and Paul*, 1992] and crustal radiogenic heat source values reduced by 1/3 below those of the cratonic Canada:  $A_1 = 1.33 \times 10^{-6}$  W/m<sup>3</sup> and  $A_2 = 0.27 \times 10^{-6}$  W/m<sup>3</sup> (see Table C1). This creates a crustal heat of 30.7 mW/m<sup>2</sup> that is used in our experiments in the presence of a mantle plume (see Table 1).

## Acknowledgments

This research was supported by funding from NASA's Sea Level Change Team, NASA's Cryospheric Science, and NASA's Earth Surface and Interior Focus Area as part of the GRACE Science Team effort. The study was performed at the Jet Propulsion Laboratory, California Institute of Technology. We thank Eric Larour for helpful discussions and suggestions and Robert B. Smith and Katrina DeNosaquo for providing data for the Yellowstone area. We are thankful to Bernard Steinberger and an anonymous reviewer for providing insightful comments that improved the quality of this manuscript. The data used are listed in the references and tables and are freely available from the corresponding author. ISSM is an open-source software available at [issm.jpl.nasa.gov](http://issm.jpl.nasa.gov).

## References

- Accardo, N. J., et al. (2014), Upper mantle seismic anisotropy beneath the West Antarctic Rift System and surrounding region from shear wave splitting analysis, *Geophy. J. Int.*, 198, 414–429, doi:10.1093/gji/ggu117.
- Aki, K., and P. G. Richards (1980), *Quantitative Seismology, Theory and Methods. Volume I and Volume II*, 208 pp., W. H. Freeman, San Francisco, Calif.
- Alley, K. E., T. A. Scambos, M. R. Siegfried, and H. A. Fricker (2016), Impacts of warm water on Antarctic ice shelf stability through basal channel formation, *Nat. Geosci.*, 9, 290–293, doi:10.1038/ngeo2675.
- An, M., D. A. Wiens, Y. Zhao, M. Feng, A. Nyblade, M. Kanao, Y. Li, A. Maggi, and J.-J. Leveque (2015), Temperature, lithosphere–asthenosphere boundary, and heat flux beneath the Antarctic Plate inferred from seismic velocities, *J. Geophys. Res. Solid Earth*, 120, 8720–8742, doi:10.1002/2015JB011917.
- Aschwanden, A., E. Bueler, C. Khroulev, and H. Blatter (2012), An enthalpy formulation for glaciers and ice sheets, *J. Glaciol.*, 58(209), 441–457, doi:10.3189/2012JoG11J088.
- Babonis, G. S., B. Csatho, and T. Schenk (2016), Mass balance changes and ice dynamics of Greenland and Antarctic ice sheets from laser altimetry, *ISPRS J. Photogramm. Remote Sens.*, 41(B8), 481–487, doi:10.5194/isprsarchives-XLI-B8-481-2016.
- Becker, T. W., A. J. Schaeffer, S. Lebedev, and C. P. Conrad (2015), Toward a generalized plate motion reference frame, *Geophys. Res. Lett.*, 42, 3188–3196, doi:10.1002/2015GL063695.
- Bell, R. E. (2008), The role of subglacial water in ice-sheet mass balance, *Nat. Geosci.*, 1(5), 297–304, doi:10.1038/ngeo186.
- Blackwell, D. (1989), Regional implications of heat flow of the Snake River Plain, northwestern United States, *Tectonophysics*, 164, 323–343, doi:10.1016/0040-1951(89)90025-5.
- Blackwell, D. D., P. T. Negaruru, and M. C. Richards (2007), Assessment of the enhanced geothermal system resource base of the United States, *Nat. Resour. Res.*, 15(4), 283–308, doi:10.1007/s11053-007-9028-7.
- Blackwell, D. D., M. Richards, Z. Frone, J. Batir, A. Ruzo, R. Dingwall, and M. Williams (2011), Temperature at depth maps for the conterminous US and geothermal resource estimate, *Geotherm. Resour. Counc. Trans.*, 35, 1545–1550.
- Blankenship, D. D., C. R. Bentley, S. T. Rooney, and D. Blackwell (1986), Seismic measurement reveal a saturated porous layer beneath an active Antarctic ice stream, *Nature*, 322(6074), 54–57, doi:10.1038/322054a0.
- Blankenship, D. D., R. E. Bell, S. M. Hodge, J. M. Brozena, J. Behrendt, and C. A. Finn (1993), Active volcanism beneath the West Antarctic Ice Sheet and implications for ice-sheet stability, *Nature*, 361, 526–529, doi:10.1038/361526a0.
- Bonneville, A., R. P. Von Herzen, and F. Lucazeau (1997), Heat flow over Reunion hot spot track: Additional evidence for thermal rejuvenation of oceanic lithosphere, *J. Geophys. Res.*, 102, 22,731–22,747.
- Bromley, G. R., M. B. L. Hall, J. O. Stone, and H. Conway (2012), Late Pleistocene evolution of Scott Glacier, southern Transantarctic Mountains: Implications for the Antarctic contribution to deglacial sea level, *Quat. Sci. Rev.*, 50, 1–13.
- Budd, W. F., D. Jenssen, and I. N. Smith (1984), A three-dimensional time-dependent model of three West Antarctic ice-sheet, *Ann. Glaciol.*, 5, 29–36.
- Busse, F. H. (1979), High Prandtl number convection, *Phys. Earth Planet. Int.*, 19, 149–157.
- Campbell, I. H., and R. W. Griffiths (1990), Implications of mantle plume structure for the evolution of flood basalts, *Earth Planet Sci. Lett.*, 99, 79–93.
- Campillo, M., and A. Paul (1992), Influence of the lower crustal structure on the early coda of regional seismograms, *J. Geophys. Res.*, 9(7), 3405–3416, doi:10.1029/91JB02714.
- Carsey, F., A. Behar, A. L. Lane, V. Realmuto, and H. Englehardt (2002), A borehole camera system for imaging the deep interior of ice sheets, *J. Glaciol.*, 48, 622–628, doi:10.3189/17275650278183112.
- Carslaw, H. S., and J. C. Jaeger (1986), *Conduction of Heat in Solids*, 2nd ed., Oxford Univ. Press, Oxfordshire, U. K.
- Carter, S. P., D. D. Blankenship, D. A. Young, M. E. Peters, J. W. Holt, and M. J. Siegert (2009), Dynamic distributed drainage implied by the flow evolution of the 1996–1998 Adventure Trench subglacial lake discharge, *Earth Planet. Sci. Lett.*, 283, 24–37, doi:10.1016/j.epsl.2009.03.019.
- Carter, S. P., H. A. Fricker, D. D. Blankenship, J. V. Johnson, W. H. Lipscomb, S. F. Price, and D. A. Young (2011), Modeling 5 years of subglacial lake activity in the MacAyeal Ice Stream (Antarctica) catchment through assimilation of ICESat laser altimetry, *J. Glaciol.*, 57(206), 1098–1112.
- Chaput, J., et al. (2014), The crustal thickness of West Antarctica, *J. Geophys. Res. Solid Earth*, 119, 378–395, doi:10.1002/2013JB010642.
- Courtillot, V., A. Davaille, J. Besse, and J. Stock (2003), Three distinct types of hotspots in the Earth's mantle, *Earth Planet. Sci. Lett.*, 205, 295–308.
- Courtney, R. C., and R. S. White (1986), Anomalous heat flow and geoid across the Cape Verde Rise: Evidence for dynamic support from a thermal plume in the mantle, *Geophys. J. R. Astron. Soc.*, 87, 815–867.

- Creyts, T. T., and C. G. Schoof (2009), Drainage through subglacial water sheets, *J. Geophys. Res.*, 114, 1–18, doi:10.1029/2008JF001215.
- Cserepes, L., and D. A. Yuen (2000), On the possibility of a second kind of mantle plume, *Earth Planet. Sci. Lett.*, 183(12), 61–71, doi:10.1016/S0012-821X(00)00265-X.
- Daly, S. F., and A. Raefsky (1985), On the penetration of a hot diapir through a strongly temperature-dependent viscosity medium, *Geophys. J. R. Astron. Soc.*, 83, 657–681.
- Dalziel, I. W. D., and L. A. Lawver (2001), The lithospheric setting of the West Antarctic Ice Sheet, in *The West Antarctic Ice Sheet: Behavior and Environment*, vol. 77, edited by R. B. Alley and R. A. Bindschadler, pp. 29–44, AGU, Washington, D. C.
- Damiani, T. M., T. A. Jordan, F. Ferraccioli, D. A. Young, and D. D. Blankenship (2014), Variable crustal thickness beneath Thwaites Glacier revealed from airborne gravimetry, possible implications for geothermal heat flux in West Antarctica, *Earth Planet. Sci. Lett.*, 407, 109–122, doi:10.1016/j.epsl.2014.09.023.
- Davies, J. H. (2013), Global map of solid Earth surface heat flow, *Geochem. Geophys. Geosyst.*, 14, 4608–4622, doi:10.1002/ggge.20271.
- DeNosaquo, K. R., R. B. Smith, and A. R. Lowry (2009), Density and lithospheric strength models of the Yellowstone-Snake River Plain volcanic system from gravity and heat flow data, *J. Volcanol. Geotherm. Res.*, 188, 108–127.
- Duval, P. (1977), The role of the water content on the creep rate of poly-crystalline ice, in *Symposium on Isotopes and Impurities in Snow and Ice*, vol. 118, pp. 29–33, International Association of Hydrological Sciences Publication, Grenoble, France.
- Eagles, G., K. Gohl, and R. D. Larter (2004), High-resolution animated tectonic reconstruction of the South Pacific and West Antarctic Margin, *Geochem. Geophys. Geosyst.*, 5, Q07002, doi:10.1029/2003GC000657.
- Emry, E. L., A. A. Nyblade, J. Julia, S. Anandakrishnan, R. C. Aster, D. A. Wiens, A. D. Huerta, and T. J. Wilson (2015), The mantle transition zone beneath West Antarctica: Seismic evidence for hydration and thermal upwellings, *Geochem. Geophys. Geosyst.*, 16, 40–58, doi:10.1002/2014GC005588.
- Engelhardt, H. (2004), Thermal regime and dynamics of the West Antarctic ice sheet, *Ann. Glaciol.*, 39, 85–92.
- Fisher, A. T., D. M. Kenneth, M. T. Slawek, W. T. Scott, F. Neil, and WISSARD Science Team (2015), High geothermal heat flux measured below the West Antarctic Ice Sheet, *Sci. Adv.*, 1, E1500093, doi:10.1126/sciadv.1500093.
- Fitzsimons, I. C. W. (2003), *Proterozoic East Gondwana: Supercontinent Assembly and Breakup*, chap. Proterozoic basement provinces in southern and southwestern Australia, and their correlation with Antarctica, *Geol. Soc. London, Spec. Publ.*, pp. 93–130.
- Fretwell, P., et al. (2013), Bedmap2: Improved ice bed, surface and thickness datasets for Antarctica, *Cryosphere*, 7(1), 375–393, doi:10.5194/tc-7-375-2013.
- Fricker, H. A., and T. Scambos (2009), Connected subglacial lake activity on lower Mercer and Whillans Ice Streams, West Antarctica, 2003–2008, *J. Glaciol.*, 55(190), 303–315.
- Fricker, H. A., T. Scambos, R. Bindschadler, and L. Padman (2007), An active subglacial water system in West Antarctica mapped from space, *Science*, 315, 1544–1548, doi:10.1126/science.1136897.
- Fricker, H. A., M. R. Siegfried, S. P. Carter, and T. A. Scambos (2016), A decade of progress in observing and modelling Antarctic subglacial water systems, *Phil. Trans. R. Soc. A*, 374, 2059, doi:10.1098/rsta.2014.0294.
- Gibert, B., U. Seipold, A. Tommasi, and D. Mainprice (2003), Thermal diffusivity of upper mantle rocks: Influence of temperature, pressure, and the deformation fabric, *J. Geophys. Res.*, 108(B8), 2359, doi:10.1029/2002JB002108.
- Granot, R., S. C. Cande, J. M. Stock, F. J. Davey, and R. W. Clayton (2010), Postspreading rifting in the Adare Basin, Antarctica: Regional tectonic consequences, *Geochem. Geophys. Geosyst.*, 11, Q08005, doi:10.1029/2010GC003105.
- Gresho, P. M., and R. L. Sani (2000), *Incompressible Flow and the Finite Element Method, Volume 1: Advection-Diffusion*, vol. 1, pp. 472, John Wiley, Hoboken, N. J.
- Griffiths, R. W. (1986), Thermals in extremely viscous fluids, including the effects of temperature-dependent viscosity, *J. Fluid Mech.*, 166, 115–138.
- Griffiths, R. W., and I. H. Campbell (1990), Stirring and structure in mantle starting plumes, *Earth Planet. Sci. Lett.*, 99, 66–78, doi:10.1016/0012-821X(90)90071-5.
- Gripp, A. E., and R. G. Gordon (2002), Young tracks of hotspots and current plate velocities, *Geophys. J. Int.*, 150, 321–361.
- Hansen, S. E., J. H. Graw, L. M. Kenyon, A. A. Nyblade, D. A. Wiens, R. C. Aster, A. D. Huerta, S. Anandakrishnan, and T. Wilson (2014), Imaging the Antarctic mantle using adaptively parameterized *P*-wave tomography: Evidence for heterogeneous structure beneath West Antarctica, *Earth Planet. Sci. Lett.*, 408, 66–78, doi:10.1016/j.epsl.2014.09.043.
- Harris, R. N., and M. K. McNutt (2007), Heat flow on hot spot swells: Evidence for fluid flow, *J. Geophys. Res.*, 112, B03407, doi:10.1029/2006JB004299.
- Heeszel, D. S., D. A. Wiens, A. A. Nyblade, S. E. Hansen, M. Kanao, M. An, and Y. Zhao (2013), Rayleigh wave constraints on the structure and tectonic history of the Gamburtsev Subglacial Mountains, East Antarctica, *J. Geophys. Res. Solid Earth*, 118, 2138–2153, doi:10.1002/jgrb.50171.
- Heeszel, D. S., et al. (2016), Upper mantle structure of central and West Antarctica from array analysis of Rayleigh wave phase velocities, *J. Geophys. Res.*, 121, 1758–1775, doi:10.1002/2015JB012616.
- Holland, D., and A. Jenkins (1999), Modeling thermodynamic ice-ocean interactions at the base of an ice shelf, *J. Phys. Oceanogr.*, 29(8), 1787–1800.
- Howard, L. (1963), Heat transport by turbulent convection, *J. Fluid Mech.*, 17, 405–432.
- Huang, H.-H., F.-C. Lin, B. Schmandt, J. Farrell, R. B. Smith, and V. C. Tsai (2015), The Yellowstone magmatic system from the mantle plume to the upper crust, *Science*, 348, 773–776, doi:10.1126/science.aaa5648.
- Husson, L., and C. P. Conrad (2012), On the location of hotspots in the framework of mantle convection, *Geophys. Res. Lett.*, 39, L17304, doi:10.1029/2012GL052866.
- Ivins, E. R., C. A. Raymond, and T. S. James (2000), The influence of 5000 year-old and younger glacial mass variability on present-day crustal rebound in the Antarctic Peninsula, *Earth Planets Space*, 52, 1023–1029, doi:10.1186/BF03352325.
- Ivins, E. R., T. S. James, J. Wahr, E. J. O. Schrama, F. W. Landerer, and K. M. Simon (2013), Antarctic contribution to sea level rise observed by GRACE with improved GIA correction, *J. Geophys. Res. Solid Earth*, 118, 3126–3141, doi:10.1002/jgrb.50208.
- Jaupart, C., S. Lebrosse, F. Lucaleau, and J.-C. Mareschal (2015), Heat and energy in the mantle of the Earth, in *Treatise on Geophysics*, 2nd ed., vol. 7, edited by G. Schubert, pp. 223–270, Elsevier, Oxford, U. K., doi:10.1016/B978-0-444-53802-4.00126-3.
- Kim, B. H., C. K. Lee, K. W. Seo, W. S. Lee, and T. Scambos (2016), Active subglacial lakes beneath the stagnant trunk of Kamb Ice Stream: Evidence of channelized subglacial flow, *Cryosphere*, 55, 573–595, doi:10.5194/tc-2016-96.
- King, S. D., and C. Adam (2014), Hotspot swells revisited, *Phys. Earth Planet. Int.*, 235, 66–83.
- Kleiner, T., M. Ruckamp, J. H. Bondzio, and A. Humbert (2015), Enthalpy benchmark experiments for numerical ice sheet models, *Cryosphere*, 9, 217–228, doi:10.5194/tc-9-217-2015.

- Kohlstedt, D. L., B. Evans, and S. J. Mackwell (1995), Strength of the lithosphere: Constraints imposed by laboratory experiments, *J. Geophys. Res.*, 100, 17,587–17,602.
- Landau, L. D., E. M. Lifshitz, and L. P. Pitaevskii (1984), *Electrodynamics of Continuous Media*, 2nd ed., vol. 8, Elsevier/Butterworth Heinemann, Boston, AMS.
- Larour, E., J. Schiermeier, E. Rignot, H. Seroussi, M. Morlighem, and J. Paden (2012a), Sensitivity analysis of Pine Island Glacier ice flow using ISSM and DAKOTA, *J. Geophys. Res.*, 117, F02009, doi:10.1029/2011JF002146.
- Larour, E., H. Seroussi, M. Morlighem, and E. Rignot (2012b), Continental scale, high order, high spatial resolution, ice sheet modeling using the Ice Sheet System Model (ISSM), *J. Geophys. Res.*, 117, F01022, doi:10.1029/2011JF002140.
- Lawver, L. A., J.-Y. Royer, D. T. Sandwell, and C. R. Scotese (1991), Evolution of the Antarctic continental margins, *Geological Evolution of Antarctic*, edited by M. R. A. Thomson, J. A. Crame, and J. W. Thomson, pp. 533–539, Cambridge Univ. Pres, New York.
- LeMasurier, W. (2006), What supports the Marie Byrd Land Dome? An evaluation of potential uplift mechanisms in a continental rift system, in *Antarctica—Contributions to Global Earth Sciences*, edited by W. LeMasurier, pp. 299–302, Springer, Berlin, doi:10.1007/3-540-32934-X37.
- LeMasurier, W. E. (2008), Neogene extension and basin deepening in the West Antarctic Rift inferred from comparisons with the East African Rift and other analogs, *Geology*, 36, 247–250, doi:10.1130/G24363A.1.
- LeMasurier, W. E., and C. A. Landis (1996), Mantle-plume activity recorded by low-relief erosion surfaces in West Antarctica and New Zealand, *Geol. Soc. Am. Bull.*, 108, 1450–1466.
- LeMasurier, W. E., and D. C. Rex (1989), Evolution of linear volcanic ranges in Marie Byrd Land, West Antarctica, *J. Geophys. Res.*, 94, 7223–7236.
- Lenaerts, J., M. Vizcaino, J. Fyke, L. van Kampenhout, and M. van den Broeke (2016), Present-day and future Antarctic ice sheet climate and surface mass balance in the Community Earth System Model, *Clim. Dyn.*, 47(5–6), 1367–1381, doi:110.1007/s00382-015-2907-4.
- Lenaerts, J. T. M., M. R. van den Broeke, W. J. van de Berg, E. van Meijgaard, and P. K. Munneke (2012), A new, high-resolution surface mass balance map of Antarctica (1979–2010) based on regional atmospheric climate modeling, *Geophys. Res. Lett.*, 39, 1–5, doi:10.1029/2011GL050713.
- Lliboutry, L. A., and P. Duval (1985), Various isotropic and anisotropic ices found in glaciers and polar ice caps and their corresponding rheologies, *Ann. Geophys.*, 3, 207–224.
- Lloyd, A. J., et al. (2015), A seismic transect across West Antarctica: Evidence for mantle thermal anomalies beneath the Bentley Subglacial Trench and the Marie Byrd Land Dome, *J. Geophys. Res. Solid Earth*, 120, 8439–8460, doi:10.1002/2015JB012455.
- Llubes, M., C. Lanseau, and F. Remy (2006), Relations between basal condition, subglacial hydrological networks and geothermal flux in Antarctica, *Earth Planet. Sci. Lett.*, 241, 655–662, doi:10.1016/j.epsl.2005.10.040.
- Lough, A. C., and et al. (2013), Seismic detection of an active subglacial magmatic complex in Marie Byrd Land, Antarctica, *Nat. Geosc.*, 6(12), 1031–1035, doi:10.1038/ngeo1992.
- MacAyeal, D. R. (1989), Large-scale ice flow over a viscous basal sediment: Theory and application to Ice Stream B, Antarctica, *J. Geophys. Res.*, 94(B4), 4071–4087.
- Malkus, W. V. R. (1954), The heat transport and spectrum of thermal turbulence, *Proc. R. Soc. London, Ser. A*, 225, 196–212.
- Mareschal, J. C., A. Nyblade, H. K. C. Perry, C. Jaupart, and G. Bienfait (2004), Heat flow and deep lithospheric thermal structure at Lac de Gras, Slave Province, Canada, *Geophys. Res. Lett.*, 31, L12611, doi:10.1029/2004GL020133.
- Maule, C. F., M. E. Purucker, N. Olsen, and K. Mosegaard (2005), Heat flux anomalies in antarctica revealed by satellite magnetic data, *Science*, 309(5733), 464–467, doi:10.1126/science.1106888.
- Maxwell, L. R., V. Lekic, and C. Lithgow-Bertelloni (2015), Viscosity jump in Earth's mid-mantle, *Science*, 350(6266), 1349–1352, doi:10.1126/science.aad1929.
- Montelli, R., G. Nolet, F. A. Dahlen, and G. Masters (2006), A catalogue of deep mantle plumes: New results from finite frequency tomography, *Geochem. Geophys. Geosyst.*, 7, Q11007, doi:10.1029/2006GC001248.
- Morlighem, M., E. Rignot, H. Seroussi, E. Larour, H. Ben Dhia, and D. Aubry (2010), Spatial patterns of basal drag inferred using control methods from a full-Stokes and simpler models for Pine Island Glacier, West Antarctica, *Geophys. Res. Lett.*, 37, L14502, doi:10.1029/2010GL043853.
- Nowicki, S., et al. (2013), Insights into spatial sensitivities of ice mass response to environmental change from the SeaRISE ice sheet modeling project I: Antarctica, *J. Geophys. Res. Earth Surf.*, 118, 1–23, doi:10.1002/jgrf.20081.
- Nyblade, A., and S. W. Robinson (1994), The African superswell, *Geophys. Res. Lett.*, 21(9), 765–768.
- Olson, P., G. Schubert, and C. Anderson (1993), Structure of axisymmetric mantle plumes, *J. Geophys. Res.*, 98, 6829–6844.
- Panter, K. S., J. Bluszatajn, S. R. Hart, P. R. Kyle, R. Esser, and W. C. McIntosh (2006), The origin of HIMU in the SW Pacific: Evidence from intraplate volcanism in Southern New Zealand and Subantarctic Islands, *J. Petrology*, 47, 1673–1704, doi:10.1093/petrology/egl024.
- Pattyn, F. (2010), Antarctic subglacial conditions inferred from a hybrid ice sheet/ice stream model, *Earth Planet. Sci. Lett.*, 295, 451–461, doi:10.1016/j.epsl.2010.04.025.
- Pattyn, F., S. P. Carter, and M. Thoma (2016), Advances in modelling subglacial lakes and their interaction with the Antarctic ice sheet, *Phil. Trans. R. Soc. A*, 374, 1–14, doi:10.1098/rsta.2014.0296.
- Pollard, D., R. DeConto, and A. A. Nyblade (2005), Sensitivity of Cenozoic Antarctic ice sheet variations to geothermal heat flux, *Global Planet. Change*, 49(1–2), 63–74, doi:10.1016/j.gloplacha.2005.05.003.
- Ramirez, C., A. Nyblade, S. E. Hansen, D. A. Wiens, S. Anandakrishnan, R. C. Aster, A. Huerta, P. Shore, and T. Wilson (2016), Crustal and upper-mantle structure beneath ice-covered regions in Antarctica from S-wave receiver functions and implications for heat flow, *Geophys. J. Int.*, 204, 1636–1648, doi:10.1093/gji/ggv542.
- Rignot, E., J. Mouginot, and B. Scheuchl (2011), Ice flow of the antarctic ice sheet, *Science*, 333(6048), 1427–1430, doi:10.1126/science.1208336.
- Rogozhina, I., J. M. Hagedorn, M. Martinec, K. Fleming, O. Soucek, R. Greve, and M. Thomas (2012), Effects of uncertainties in the geothermal heat flux distribution on the Greenland ice sheet: An assessment of existing heat flow models, *J. Geophys. Res.*, 117, F02025, doi:10.1029/2011JF002098.
- Rogozhina, I., et al. (2016), Melting at the base of the Greenland ice sheet explained by Iceland hotspot history, *Nat. Geosc.*, 9, 366–373, doi:10.1038/NGEO2689.
- Schmandt, B., K. G. Dueker, E. D. Humphreys, and S. H. Hansen (2012), Hot mantle upwelling across the 660 beneath Yellowstone, *Earth Planet. Sci. Lett.*, 331–332, 224–236, doi:10.1016/j.epsl.2012.03.025.
- Schroeder, D. M., D. D. Blankenship, and D. A. Young (2013), Evidence for a water system transition beneath Thwaites Glacier, West Antarctica, *Proc Natl. Acad. Sci. U.S.A.*, 110(30), 12,225–12,228, doi:10.1073/pnas.1302828110.

- Schroeder, D. M., D. D. Blankenship, D. A. Young, and E. Quartini (2014), Evidence for elevated and spatially variable geothermal flux beneath the West Antarctic Ice Sheet, *Proc. Natl. Acad. Sci. U.S.A.*, 111(25), 9070–9072, doi:10.1073/pnas.1405184111.
- Schroeder, D. M., H. Seroussi, W. Chu, and D. A. Young (2016), Adaptively constraining radar attenuation and temperature across the Thwaites Glacier catchment using bed echoes, *J. Glaciol.*, 62(236), 1075–1082, doi:10.1017/jog.2016.100.
- Seroussi, H., M. Morlighem, E. Rignot, A. Khazendar, E. Larour, and J. Mouginot (2013), Dependence of century-scale projections of the Greenland ice sheet on its thermal regime, *J. Glaciol.*, 59(218), 1024–1034, doi:10.3189/2013JoG13J054.
- Seroussi, H., M. Morlighem, E. Rignot, J. Mouginot, E. Larour, M. P. Schodlok, and A. Khazendar (2014), Sensitivity of the dynamics of Pine Island Glacier, West Antarctica, to climate forcing for the next 50 years, *Cryosphere*, 8(5), 1699–1710, doi:10.5194/tc-8-1699-2014.
- Shapiro, N. M., and M. H. Ritzwoller (2002), Monte-Carlo inversion for a global shear-velocity model of the crust and upper mantle, *Geophys. J. Int.*, 151, 88–105.
- Shapiro, N. M., and M. H. Ritzwoller (2004), Inferring surface heat flux distributions guided by a global seismic model: Particular application to Antarctica, *Earth Planet. Sci. Lett.*, 223(1–2), 213–224, doi:10.1016/j.epsl.2004.04.011.
- Siegert, M. J., and J. A. Dowdeswell (1996), Spatial variations in heat at the base of the Antarctic ice sheet from analysis of the thermal regime above subglacial lakes, *J. Glaciol.*, 42(142), 501–509.
- Siegfried, M. R., H. A. Fricker, M. Roberts, T. A. Scambos, and S. Tulaczyk (2014), A decade of West Antarctic subglacial lake interactions from combined ICESat and CryoSat-2 altimetry, *Geophys. Res. Lett.*, 41, 891–898, doi:10.1002/2013GL058616.
- Siegfried, M. R., H. A. Fricker, S. P. Carter, and S. Tulaczyk (2016), Episodic ice velocity fluctuations triggered by a subglacial flood in West Antarctica, *Geophys. Res. Lett.*, 43, 2640–2648, doi:10.1002/2016GL067758.
- Sieminski, A., E. Debyale, and J.-J. Lévéque (2003), Seismic evidence for deep low-velocity anomalies in the transition zone beneath West Antarctica, *Earth Planet. Sci. Lett.*, 216(4), 645–661, doi:10.1016/S0012-821X(03)00518-1.
- Sleep, N. H. (1990), Hotspots and mantle plumes: Some phenomenology, *J. Geophys. Res.*, 95(B5), 6715–6736, doi:10.1029/JB095iB05p06715.
- Smith, B. E., H. A. Fricker, I. R. Joughin, and S. Tulaczyk (2009), An inventory of active subglacial lakes in Antarctica detected by ICESat (2003–2008), *J. Glaciol.*, 55(192), 573–595.
- Smith, R. B., M. Jordan, B. Steinberger, C. M. Puskas, J. Farrell, G. P. Waite, S. Husen, W.-L. Chang, and R. J. O'Connell (2009), Geodynamics of the Yellowstone hotspot and mantle plume: Seismic and GPS imaging, kinematics, and mantle flow, *J. Volcanol. Geotherm. Res.*, 188, 26–56, doi:10.1016/j.volgeores.2009.08.020.
- Spasojevic, S., M. Gurnis, and R. Sutherland (2010), Mantle upwellings above slab graveyards linked to the global geoid lows, *Nat. Geosci.*, 3, 435–438, doi:10.1038/ngeo855.
- Steinberger, B. (2000), Slabs in the lower mantle results of dynamic modeling compared with tomographic images and the geoid, *Phys. Earth Planet. Inter.*, 118, 241–257.
- Storey, B. C., P. T. Leat, S. D. Weaver, J. D. Pankhurst, and S. Kelley (1999), Mantle plumes and Antarctica-New Zealand rifting: Evidence from mid-Cretaceous mafic dikes, *J. Geol. Soc.*, 156, 659–671, doi:10.1144/gsjgs.156.4.0659.
- Storey, B. C., A. P. M. Vaughan, and T. R. Riley (2013), The links between large igneous provinces, continental break-up and environmental change: Evidence reviewed from Antarctica, *Earth Environ. Sci. Trans. R. Soc. Edinburgh*, 104, 1–14.
- Sutherland, R., S. Spasojevic, and M. Gurnis (2010), Mantle upwelling after Gondwana subduction death explains anomalous topography and subsidence histories of eastern New Zealand and West Antarctica, *Geology*, 38, 155–158, doi:10.1130/G30613.1.
- Torsvik, T. H., C. Gainaand, and T. F. Redfield (2008), Antarctica and global paleogeography: From Rodinia, through Gondwanaland and Pangea, to the birth of the Southern Ocean and the opening of gateways, in *Antarctica: A Keystone in a Changing World. Proceedings of the 10th International Symposium on Antarctic Earth Sciences*, edited by A. K. Cooper et al., pp. 125–140, National Acad. Press, Washington, D. C., doi:10.3133/of2007-1047.kp11.
- Turner, J. S. (1973), *Buoyancy Effects in Fluids*, Cambridge Univ. Press, U. K.
- Van Keken, P. (1997), Evolution of starting mantle plumes: A comparison between numerical and laboratory models, *Earth Planet. Sci. Lett.*, 148, 1–11, doi:10.1016/S0012-821X(97)00042-3.
- Weaver, S. D., B. Storey, R. J. Pankhurst, S. B. Mukasa, V. J. Divenere, and J. D. Bradshaw (1994), Antarctica-New Zealand rifting and Marie Byrd Land lithospheric magmatism linked to ridge subduction and mantle plume activity, *Geology*, 22(B4), 811–814, doi:10.1029/97JB00266.
- Weinberg, R. F. (1997), Rise of starting plumes through the mantle of temperature and pressure-dependent viscosity, *J. Geophys. Res.*, 102, 7613–7623.
- Winberry, J. P., and S. Anandakrishnan (2004), Crustal structure of the West Antarctic Rift System and Marie Byrd Land hotspot, *Geology*, 32(11), 977–980, doi:10.1130/G20768.1.
- Winberry, J. P., S. Anandakrishnan, and R. Alley (2009), Seismic observations of transient subglacial water-flow beneath MacAyeal Ice Stream, West Antarctica, *Geophys. Res. Lett.*, 36, L11502, doi:10.1029/2009GL037730.
- Yokoyama, Y., et al. (2016), Widespread collapse of the Ross Ice Shelf during the late Holocene, *Proc. Natl. Acad. Sci. U.S.A.*, 113(9), 2354–2359, doi:10.1073/pnas.1516908113.
- Yoshida, M. (2012), Plumes buoyancy and heat fluxes from the deep mantle estimated by an instantaneous mantle flow simulation based on the S4ORTS global seismic tomography model, *Physics Earth Planet. Inter.*, 210–211, 63–74, doi:10.1016/j.pepi.2012.08.006.
- Young, D. A., D. M. Schroeder, D. D. Blankenship, S. D. Kempf, and E. Quartini (2016), The distribution of basal water between Antarctic subglacial lakes from radar sounding, *Phil. Trans. R. Soc. A*, 374(20140297), doi:10.1098/rsta.2014.0297.
- Zhao, D. (2015), *Multiscale Seismic Tomography*, 304 pp., Springer Geophys. Ser., Japan.